



1 **Chemical Composition-Dependent Hygroscopic Behavior of Individual Ambient Aerosol**  
2 **Particles Collected at a Coastal Site**

3

4 Li Wu<sup>1,2,+</sup>, Hyo-Jin Eom<sup>1,3,+</sup>, Hanjin Yoo<sup>1,4</sup>, Dhruvajyoti Gupta<sup>1</sup>, Hye-Rin Cho<sup>1</sup>, Pingqing Fu<sup>2</sup>, and  
5 Chul-Un Ro<sup>1,4,\*</sup>

6

7 <sup>1</sup>Department of Chemistry, Inha University, Incheon 22212, Korea

8 <sup>2</sup>Institute of Surface-Earth System Science, School of Earth System Science, Tianjin University,  
9 Tianjin 300072, China

10 <sup>3</sup>Air Quality Research Division, National Institute of Environmental Research, Incheon 22689, Korea

11 <sup>4</sup>Particle Pollution Management Center, Inha University, Incheon 21999, Korea

12

13 \* *Correspondence to* Chul-Un Ro ([curo@inha.ac.kr](mailto:curo@inha.ac.kr))

14 <sup>+</sup>Authors with equal contributions

15

16 **Abstract**

17 This study investigated the hygroscopic behavior of individual ambient aerosol particles  
18 collected at a coastal site of Jeju Island, Korea. The particles' size change along with phase transitions  
19 during humidification and dehydration processes, and their chemical compositions, were determined  
20 by optical microscopy and scanning electron microscopy-energy dispersive X-ray spectroscopy (SEM-  
21 EDX), respectively. Of the 39 particles analyzed, 24 were aged sea-spray aerosols (SSAs) with diverse  
22 mixing ratios of Cl<sup>-</sup> and NO<sub>3</sub><sup>-</sup>.

23 The ambient SSAs exhibited multiple deliquescence and efflorescence transitions that were  
24 dominantly influenced by NaCl, NaNO<sub>3</sub>, MgCl<sub>2</sub>, Mg(NO<sub>3</sub>)<sub>2</sub> and organic species covering the surface  
25 of the aged SSAs. For Cl-rich SSAs with  $X_{(\text{Na}, \text{Mg})\text{Cl}} > 0.4$ , although some particles showed very slow  
26 water uptake at low RHs = ~30%, two major transitions were observed during the humidification  
27 process, firstly at RH = ~63.8%, regardless of their chemical compositions, which is the mutual  
28 deliquescence relative humidity (MDRH), and secondly at RH = 67.5–73.5%, depending on their  
29 chemical compositions, which are the final DRHs. During the dehydration process, the Cl-rich SSAs  
30 showed single-stage efflorescence at RH = 33.0–50.5%, due to simultaneous heterogeneous  
31 crystallization of inorganic salts. For Cl-depleted SSAs with  $X_{(\text{Na}, \text{Mg})\text{Cl}} < 0.4$ , two prompt deliquescence



32 transitions were observed during the humidification process, firstly at MDRH = 63.8 % and secondly  
33 at RH = 65.4–72.9%. The mutual deliquescence transition was more distinguishable for Cl-depleted  
34 SSAs. During the dehydration process, step-wise transitions were observed at efflorescence RHs (ERHs)  
35 = 24.6–46.0% and 17.9–30.5%, depending on their chemical compositions.

36 Additionally, aged mineral particles showed partial or complete phase changes with varying  
37 RH due to the presence of SSAs and/or  $\text{NO}_3^-$  species. In contrast, non-reacted mineral and Fe-rich  
38 particles maintained their size during the entire hygroscopic process. The mixture particles of organic  
39 and ammonium sulfate (AS) exhibited lower deliquescence and efflorescence RHs compared to pure  
40 AS salt, highlighting the impact of organic species on the hygroscopic behavior of AS. These findings  
41 emphasize the complexity of atmospheric aerosols and the importance of considering their composition  
42 and mixing state when modeling their hygroscopic behavior and subsequent atmospheric impacts.

43

## 44 **1 Introduction**

45 Atmospheric aerosols play a significant role in the global climate by directly scattering or  
46 absorbing incoming solar radiation and indirectly serving as cloud condensation nuclei (Pandis et al.,  
47 1995; Haywood and Boucher, 2000). The hygroscopicity of ambient aerosol particles, critically  
48 depending on their compositions, is of vital importance in understanding their properties, including  
49 their effects on aerodynamic performance, cloud-droplet nucleation efficiency, optical properties, and  
50 heterogeneous chemical reactivity with atmospheric gas-phase species. (Ten Brink, 1998; Krueger et  
51 al., 2003; Wang and Martin, 2007; Wu et al., 2020). However, the study of their hygroscopic behavior  
52 is challenging because ambient aerosols typically exist as complex mixtures of several chemical species,  
53 even at the individual particle level, due to multiphase interactions (Krieger et al., 2012; Pöschl and  
54 Shiraiwa, 2015; Schiffer et al., 2018).

55 Sea-spray aerosols (SSAs) are a significant component comprising 25-60% of atmospheric  
56 particulate matter mass (Finlayson-Pitts and Pitts, 2000; Song et al., 2022). Understanding the  
57 hygroscopic properties of SSAs is essential for study on aerosol-cloud interactions and global climate  
58 (Schill et al., 2015; Zieger et al., 2017), which however, is still defective owing to their complex  
59 chemical compositions (Meskhidze et al., 2013; Xu et al., 2020; Cochran et al., 2017). Nascent SSAs  
60 are formed when bubbles burst at the sea surface, generating both submicron and supermicron SSAs  
61 from film and/or jet drops (Quinn et al., 2015; Wang et al., 2017). The primary inorganic constituents  
62 of nascent SSAs are  $\text{Na}^+$ ,  $\text{Cl}^-$ , and  $\text{Mg}^{2+}$ , followed by  $\text{SO}_4^{2-}$ ,  $\text{Ca}^{2+}$ ,  $\text{K}^+$ , and other minor compositions



63 (Seinfeld and Pandis, 2006). Submicron nascent SSAs contain more organic species and fewer  
64 inorganic salts than supermicron ones (Ault et al., 2013; Prather et al., 2013; Wang et al., 2015). In  
65 pristine marine environments, the organics in SSAs mostly originate from phytoplankton activities in  
66 the sea, while in polluted marine environments, non-biodegradable surfactants from anthropogenic  
67 waste run-offs to the sea are supposed to be added (Cochran et al., 2016; Forestieri et al., 2016).  
68 Reactions of SSAs with various atmospheric species, such as  $\text{NO}_x/\text{HNO}_3$ ,  $\text{SO}_2/\text{H}_2\text{SO}_4$ , and  $\text{CH}_3\text{SO}_3\text{H}$ ,  
69 within minutes to hours of residence in air further increase the complexity of the chemical compositions  
70 (ten Brink, 1998; Saul et al., 2006; Liu et al., 2007), leading to partially or fully reacted (or aged) SSAs  
71 after Cl depletion (Pósfai et al., 1995; Gard et al., 1998; Laskin et al., 2012; Ault et al., 2014; Wu et al.,  
72 2020). The further reactive uptake of  $\text{N}_2\text{O}_5$  was also reported to be dependent on the chloride to nitrate  
73 ratio of the reacted SSAs and their phases (Ryder et al., 2014). In addition, SSAs interact with volatile  
74 organic carbons (VOCs), secondary organic aerosols (SOAs), etc., in the marine boundary layer (Su et  
75 al., 2022). The presence of primary and secondary organics, biogenic species, sea-salt sulfates (ss-  
76  $\text{SO}_4^{2-}$ ), non-sea-salt sulfates (nss- $\text{SO}_4^{2-}$ ), etc., adds greater complexity to the interdependence of  
77 hygroscopic behavior and heterogeneous reactions in ambient SSAs (Keene et al., 2007; O'Dowd and  
78 de Leeuw, 2007; Ault et al., 2013; Beardsley et al., 2013; Prather et al., 2013).

79 Many studies have investigated the hygroscopic behavior of both airborne and laboratory-  
80 generated SSAs. It is generally accepted that sea-salt-containing particles result in higher hygroscopic  
81 factors in supermicron particles (Atkinson et al., 2015; Herich et al., 2009). Some single particle  
82 measurements have been reported on ambient fine and coarse mode SSAs that are dominated by  
83 inorganic salt species. For example, environmental transmission electron microscopy was used to  
84 measure the deliquescence and efflorescence relative humidities (DRHs and ERHs) of NaCl-bearing  
85 aerosols, sulfate/chloride containing SSAs, Mg-rich particles, etc., collected from clean and polluted  
86 environments (Wise et al., 2007; Semeniuk et al., 2007). It was found that NaCl moiety in  
87 sulfate/chloride containing SSAs underwent deliquescence at ~75% RH with the sulfate-bearing phases  
88 remaining insoluble, which is similar to the DRH of pure NaCl aerosols, whereas the DRH of the NaCl  
89 moiety was lowered in the presence of soluble compositions like  $\text{NaNO}_3$ . In a follow-up study, the  
90 DRHs and ERHs of laboratory-generated and ambient SSA particles were found to be consistent (Wise  
91 et al., 2009). Similar observations for marine aerosols with insoluble sulfate moieties and a highly  
92 hygroscopic NaCl-moiety were also reported (Freney et al., 2010a). In-situ Raman spectrometry was  
93 used to probe the phase transitions of SSA droplets (80–100  $\mu\text{m}$ ) nebulized from sea-water, which



94 revealed that  $\text{CaSO}_4 \cdot 0.5\text{H}_2\text{O}$  solidified at  $\text{RH} > 90\%$ , followed by crystallizations of NaCl and  
95  $\text{KMgCl}_3 \cdot 6\text{H}_2\text{O}$  at  $\text{RH} = \sim 55\%$  and  $\sim 44\%$ , respectively (Xiao et al., (2008). Optical microscopy  
96 combined with low-Z particle energy-dispersive electron probe X-ray microanalysis (low-Z particle  
97 EPMA) was used to determine 2-D growth factors, phase transition RHs, and chemical compositions  
98 in ambient aerosols, including nascent and reacted/aged SSAs (Ahn et al., 2010). However, the  
99 relationship between hygroscopic properties and the evolving chemical compositions and mixing states  
100 of ambient SSAs remains unclear.

101 Laboratory-generated inorganic salt particles have been utilized as surrogates to understand and  
102 parameterize the complex hygroscopic properties of SSAs for climate models. Since NaCl constitutes  
103 approximately 80% of nascent SSAs by mass, the hygroscopic behavior of pure NaCl particles has been  
104 extensively studied for parameterizing the thermodynamic and optical properties and cloud activation  
105 efficiency of ambient SSAs (Tang et al., 1997; Niedermeier et al., 2008). However, the hygroscopic  
106 growth factors of ambient or laboratory-generated SSAs are reported to be different from those of pure  
107 NaCl, possibly due to the presence of hydrates such as  $\text{MgCl}_2 \cdot 6\text{H}_2\text{O}$ , organic substances, or other  
108 impurities (Ahn et al., 2010; Schindelholz et al., 2014; Zieger et al., 2017; Rosati et al., 2021; Guo et  
109 al., 2019; Kong et al., 2018). Consequently, the hygroscopic properties of multicomponent systems  
110 such as mixed cation chlorides (Ge et al., 1996, 1998; Chan et al., 2000; Li et al., 2014b; Gupta et al.,  
111 2015a), sodium salts of mixed anions (Gupta et al., 2015b; Chang and Lee, 2002; Freney et al., 2010b;  
112 Chan et al., 1997), and other mixture systems such as NaCl-MgSO<sub>4</sub> (Woods et al., 2010), NaCl-CaSO<sub>4</sub>  
113 (Freney et al., 2010b), NaCl-(NH<sub>4</sub>)<sub>2</sub>SO<sub>4</sub> (Tobon et al., 2021) are of special relevance, which can serve  
114 as surrogates for ambient or reacted SSAs.

115 As discussed in detail elsewhere (Li et al., 2014b; Gupta et al., 2015b), equilibrium  
116 thermodynamics state that binary mixture systems such as NaCl-KCl, NaCl-MgCl<sub>2</sub>, and NaCl-NaNO<sub>3</sub>  
117 exhibit multi-stage deliquescence/efflorescence transitions at mutual DRHs/ERHs (MDRHs/MERHs)  
118 due to the dissolution/crystallization of eutonic compositions, which are independent of the initial  
119 mixing ratios, and at specific DRHs/ERHs due to the richer salt moiety, respectively. Thermodynamic  
120 models, such as the Extended Atmospheric Inorganics Model (E-AIM)  
121 (<http://www.aim.env.uea.ac.uk/aim/aim.php>; (Ansari and Pandis, 1999; Carslaw et al., 1995; Clegg et  
122 al., 1998a, b; Wexler and Clegg, 2002) and the Aerosol Inorganic-Organic Mixtures Functional groups  
123 Activity Coefficients (AIOMFAC) (<http://www.aiomfac.caltech.edu>; Zuend et al., 2008, 2011), can  
124 predict MDRHs and DRHs for multicomponent mixture systems. However, as efflorescence is a kinetic



125 or rate-driven process, no general theoretical model can predict the efflorescence of single or  
126 multicomponent aerosol particles, and thus the best way is experimental observation (Seinfeld and  
127 Pandis, 2006; Cohen et al., 1987; Martin, 2000). Previous modeling and field studies have attributed  
128 the reduction in hygroscopic growth of SSAs to the organic fractions (Ming and Russell, 2001; Vaishya  
129 et al., 2013; Zhang et al., 2014), whereas recent measurements suggest that organic species have an  
130 insignificant influence (Nguyen et al., 2017). Therefore, establishing a systematic correlation between  
131 the chemical compositions and hygroscopic behavior of ambient SSAs vis-à-vis the multicomponent  
132 inorganic surrogates is a priority towards understanding the hygroscopic properties of ambient SSAs  
133 and parametrizing phase changes for model applications.

134 Mineral particles, such as aluminosilicates and calcium carbonate, which are typically non-  
135 hygroscopic, can become hygroscopic when they are internally mixed with SSAs or react with gaseous  
136 species such as NO<sub>x</sub>, SO<sub>2</sub>, and organic acids in the presence of water vapor (Tang et al., 2016; Li et al.,  
137 2014a). In fact, mineral dust and aged SSAs may exist as internal and/or external mixtures in the  
138 atmosphere (Geng et al., 2014). For instance, Mg-silicate particle coagulated with SSA partially  
139 increased in size only at the SSA region with increasing RH and was covered with an aqueous droplet  
140 caused by the complete dissolution of the SSA part in high RH (Semeniuk et al., 2007). Additionally,  
141 aluminosilicates coated with sulfur-bearing materials or internally mixed with sea salt particles can  
142 absorb water, although the aluminosilicates remained as solid phases (Freney et al., 2010b).

143 In this study, we systematically investigated the hygroscopic behavior of ambient aerosols  
144 collected on Jeju Island, Korea, together with their chemical compositions in various mixing states on  
145 a single particle basis. Especially, the hygroscopic properties and chemical compositions of ambient  
146 SSAs were examined and compared with multicomponent inorganic surrogate systems containing Na<sup>+</sup>,  
147 Mg<sup>2+</sup>, Cl<sup>-</sup>, and NO<sub>3</sub><sup>-</sup>. The phase transitions were observed by monitoring the 2-D size changes of the  
148 particles as a function of RH under optical microscopy and the hygroscopic curves and phase diagrams  
149 were derived. To determine the chemical compositions of the individual ambient aerosols and the  
150 spatial distribution of elements in the effloresced particles, we used scanning electron  
151 microscopy/energy dispersive X-ray spectroscopy (SEM/EDX) and analyzed their X-ray spectra and  
152 maps, respectively. Although ambient aerosols are complex in their compositions and hygroscopic  
153 properties, the detailed elucidation of their hygroscopic behavior according to chemical compositions  
154 of ambient aerosols can contribute to the ongoing efforts to improve our understanding of atmospheric  
155 aerosols and their impacts on global climate.



156 **2 Experimental Section**

157 **2.1 Samples**

158 **Ambient aerosol particles**

159 Aerosol samples were collected on April 16 and 17, 2012, at the Gosan meteorological site  
160 (33.29°N, 126.16°E) located on the west coast of Jeju Island in South Korea (see Fig. 1). Ambient  
161 aerosols were loaded on TEM grids (200-mesh Cu coated with Formvar stabilized with carbon, Ted  
162 Pella, Inc.) mounted on stages 2 and 3 of a three-stage cascade PM<sub>10</sub> impactor (Dekati Ltd.) with  
163 aerodynamic cut-off diameters of 10–2.5 μm and 2.5–1.0 μm, respectively, at a flow rate of 10 L min<sup>-1</sup>.  
164 Sampling durations for each stage were adjusted to collect an appropriate number of particles without  
165 overloading. Stage 2 particles, which were sized between 10-2.5 μm, were used to measure chemical  
166 composition and hygroscopic behavior in this study.

167

168 **Laboratory-generated (Na, Mg)(Cl, NO<sub>3</sub>) mixture particles**

169 In the previous studies (Zhang et al., 2004; Gupta et al., 2015a; Gupta et al., 2015b), aerosols  
170 of NaCl, NaNO<sub>3</sub>, Mg(NO<sub>3</sub>)<sub>2</sub>, NaCl-NaNO<sub>3</sub>, and NaCl-MgCl<sub>2</sub> were extensively investigated. As Na<sup>+</sup>,  
171 Mg<sup>2+</sup>, Cl<sup>-</sup>, and NO<sub>3</sub><sup>-</sup> are also major species of most ambient SSAs, we measured the hygroscopic  
172 behavior of NaCl-MgCl<sub>2</sub>-NaNO<sub>3</sub>-Mg(NO<sub>3</sub>)<sub>2</sub> in this work to study the hygroscopic behavior of ambient  
173 SSAs that contain similar major elements. Pure solutions (1.0 M each) of NaCl (>99.9% purity, Aldrich),  
174 MgCl<sub>2</sub>·6H<sub>2</sub>O, and NaNO<sub>3</sub> (99.9% purity, Aldrich) were prepared using de-ionized water (18 MΩ,  
175 Millipore Direct-QTM). The pure solutions were then mixed to obtain mixture solutions with  
176 [Cl<sup>-</sup>]:[NO<sub>3</sub><sup>-</sup>] = 3:1, 1:1, and 1:3 (i.e.  $X_{(Na,Mg)Cl} = 0.75, 0.5, \text{ and } 0.25$ ) while the sea water ratio of [Na<sup>+</sup>]:  
177 [Mg<sup>2+</sup>] = 9:1 was maintained. A single jet atomizer (HCT4810) was used to generate aerosol particles  
178 from the mixture solutions on hydrophobic TEM grids. Herein, a notation system is used to represent  
179 aerosol particles of NaCl-MgCl<sub>2</sub>-NaNO<sub>3</sub>-Mg(NO<sub>3</sub>)<sub>2</sub> as (Na, Mg)(Cl, NO<sub>3</sub>).

180

181 **2.2 Hygroscopic property measurements**

182 The experimental setup for measuring hygroscopic behavior consists of three main components:  
183 (A) a see-through impactor, (B) an optical microscope, and (C) a humidity control system. The TEM  
184 grid with aerosol particles was attached to the impaction plate in the see-through impactor, and the RH  
185 was controlled by mixing dry and wet gaseous N<sub>2</sub> (99.999% purity) flows that were adjusted to obtain  
186 the desired RH in the range of ~5.0–92.0%. The humidity control system used wet N<sub>2</sub> gas obtained by



187 bubbling through deionized water reservoirs. The RH was monitored by a digital hygrometer (Testo  
188 645) that was calibrated using a dew-point hygrometer (M2 Plus-RH, GE) to provide RH readings with  
189  $\pm 0.5\%$  reproducibility. A detailed discussion of the impactor and humidity-controlling system can be  
190 found elsewhere (Li et al., 2021). The particles were continuously imaged in RH = 1% steps using a  
191 digital camera (Canon EOS 5D, full frame, Canon EF f/3.5 L macro USM lens) mounted on an optical  
192 microscope (Olympus, BX51M) during the humidification process (by increasing RH from  $\sim 5.0$  to  
193  $92.0\%$ ), followed by the dehydration process (by decreasing RH from  $\sim 92.0$  to  $5.0\%$ ). The changes in  
194 particle size with the variation of RH were monitored by measuring the particle areas in the optical  
195 images to generate hygroscopic curves. Each humidity condition was sustained for at least 2 mins to  
196 allow for sufficient time for water condensation or evaporation. The hygroscopic curves are represented  
197 by the area ratio ( $A/A_0$ ) as a function of RH, where the 2-D projected aerosol area at a given RH ( $A$ ) is  
198 divided by that before starting the humidification process ( $A_0$ ). The images were processed using image  
199 analysis software (Matrox, Inspector v9.0). The experiments were conducted at room temperature ( $T =$   
200  $22 \pm 1\text{ }^\circ\text{C}$ ). Pure NaCl particles were used to verify the accuracy of the system with DRH =  $75.5 (\pm$   
201  $0.5)\%$  and ERH =  $46.3\text{--}47.6\%$ .

202

### 203 **2.3 Low-Z particle EPMA measurements using SEM-EDX**

204 The ambient aerosol particles were analyzed using low-Z particle EPMA measurements with a  
205 Jeol JSM-6390 SEM equipped with an Oxford Link super atmospheric thin window (SATW) EDX  
206 detector. The analysis was conducted both before and after the hygroscopic processes to determine the  
207 morphology, chemical composition, and spatial distribution of the chemical elements (elemental maps).  
208 The resolution of the detector was 133 eV for Mn  $K\alpha$  X-rays. Point mode and area mode X-ray spectra  
209 and elemental maps of individual particles were recorded using Oxford INCA Energy software. An  
210 accelerating voltage of 10 kV and beam current of 0.5 nA were used, and typical measurement durations  
211 were 20 sec. for point mode, 1 min. for area mode, and 5-10 min. for elemental mapping.

212 The AXIL program was used to obtain the net X-ray intensities for chemical elements through  
213 non-linear least-squares fitting of the spectra. From these intensities, the elemental concentrations of  
214 individual particles were determined (Vekemans et al., 1994). For individual particles sitting on TEM  
215 grids, C and O concentrations were determined using a Monte Carlo calculation technique to correct  
216 for the interfering X-ray peaks of C and O emitted from the TEM grid, providing accurate quantification





217 results (Geng et al., 2010). A detailed explanation of the elemental quantification procedure can be  
218 found elsewhere (Wu et al., 2019a).

219

### 220 **3 Results and Discussion**

#### 221 **3.1 Chemical compositional analysis of individual ambient aerosol particles**

222 Firstly, low-Z particle EPMA measurement was performed to find out fields on TEM grids with  
223 well-separated particles based on their secondary electron images (SEIs,  $\sim 100 \mu\text{m} \times 100 \mu\text{m}$  for a field)  
224 before conducting the hygroscopic study and chemical compositional analysis of individual ambient  
225 aerosols. The particles on the selected fields were monitored using an optical microscope at varying  
226 RHs during the humidification and dehydration processes to study their hygroscopic behavior.  
227 Subsequently, the effloresced particles were transferred back to SEM-EDX to obtain their SEIs and X-  
228 ray spectra. In this study, a total of 39 particles on three fields were investigated, including 24 SSAs  
229 with diverse mixing ratios of  $\text{Cl}^-$  and  $\text{NO}_3^-$  and 15 other particles such as six aluminosilicates, five Ca-  
230 containing particles, two Fe-rich particles, an aged  $\text{SiO}_2$ , and a mixture particle of organic and  
231  $(\text{NH}_4)_2\text{SO}_4$ . The mole fraction of Cl as  $X_{(\text{Na},\text{Mg})\text{Cl}}$  in the aged/reacted SSAs was calculated based on  
232  $[\text{Cl}^-]/([\text{Na}^+] + 2[\text{Mg}^{2+}])$  to determine the degree of Cl-depletion in the SSA particles. Fig. 2 shows the  
233 SEI of the first field containing 16 particles, where the chemical species of each particle are indicated,  
234 together with two exemplar X-ray spectra of aged SSAs #5 and #11 with  $X_{(\text{Na},\text{Mg})\text{Cl}} = 0.75$  and 0.23,  
235 respectively. The elemental concentrations of all particles and their chemical species, determined by X-  
236 ray spectral analysis, are listed in Table S1 of Supporting Information.

237

#### 238 **3.2 Hygroscopic behavior of ambient aerosol particles**

239 The hygroscopic behavior of all 39 particles was investigated in detail, in conjunction with their  
240 chemical compositional analysis. In Fig. 3, optical images obtained at different RHs during the  
241 humidification and dehydration processes and the SEI after hygroscopic process for 16 particles on the  
242 first field are shown. Except particles #2, #4, #7, #8, and #14, the rest are aged SSAs. Optical images  
243 and the SEIs for particles on the second and third fields are provided in Figs. S1 and S2, respectively.

244 Particles were initially solid at  $\text{RH} = 5.3 \%$  before the hygroscopic measurement, as shown in  
245 Fig. 3A. During the humidification process, most of the SSAs showed partial deliquescence at  $\text{RH} =$   
246  $63.8 \%$  (Fig. 3C), regardless of their aging degree, indicating the realization of the MDRH. Upon further  
247 increase of RH, SSAs underwent full deliquescence transitions at  $\text{DRH} = 65.4 - 73.5 \%$ , which varied





248 for each SSA, as shown in Figs. 3D and E. The SSA droplets showed hygroscopic growth when RH  
249 increased further as shown in Fig. 3F. During the dehydration process, almost all SSAs exhibited  
250 colored ring-type patterns (Figs. 3G and H) due to the diffraction of visible light typically observed in  
251 the presence of organic surfactants on water, indicating the presence of considerable amounts of organic  
252 species in aged SSAs. SSA droplet #5 crystallized at ERH = 50.5 % (Fig. 3G), while the others  
253 effloresced over a lower range of ERH = 46.0 – 17.9%. The various DRHs and ERHs indicate different  
254 chemical compositions of SSAs.

255 Aluminosilicates and Fe-rich particles did not exhibit any water uptake or changes as a function  
256 of RH. Aged aluminosilicates, aged SiO<sub>2</sub>, and some reacted Ca-containing particles showed modest  
257 growth/shrinkage continuously due to the presence of amorphous NO<sub>3</sub><sup>-</sup> phases (Ahn et al., 2010). The  
258 mixture particle of organic and ammonium sulfate experienced distinct deliquescence and efflorescence.  
259 Detailed description of hygroscopic behavior of the ambient aerosol particles is given as follows.

260

### 261 3.3 SSA particles

262 The average atomic concentrations of C, Na, Cl, N, Mg, S, K, and Ca in SSAs are listed in Table  
263 S1 with the values being 43.0(±7.2)%, 13.6(±4.6)%, 8.0(±6.6)%, 7.9(±2.3)%, 1.5(±0.4)%, 0.8(±0.3)%,  
264 0.3(±0.1)%, and 0.3(±0.1)%, respectively. The elemental analysis of the SSAs indicates that they  
265 consist primarily of Na<sup>+</sup>, Mg<sup>2+</sup>, Cl<sup>-</sup>, NO<sub>3</sub><sup>-</sup>, and organic species. As the SSAs become more aged or  
266 reacted, their mole fractions of Cl<sup>-</sup> relative to Na<sup>+</sup> and Mg<sup>2+</sup> decrease, while their mole fractions of NO<sub>3</sub><sup>-</sup>  
267 increase. Although the aged/reacted SSAs are a complicated multi-component system, (Na,Mg)(Cl,  
268 NO<sub>3</sub>) mixture system is considered as an inorganic surrogate system for understanding their  
269 hygroscopic behavior. The AIOMFAC model predicts the eutonic compositions of Na(Cl, NO<sub>3</sub>) and  
270 (Na, Mg)(Cl, NO<sub>3</sub>) mixture systems as  $X_{\text{NaCl}} = 0.38$  and  $X_{(\text{Na,Mg})\text{Cl}} = 0.46$ , respectively. The mole  
271 fraction of Cl in the eutonic compositions of the inorganic component of the aged SSAs would be  
272 around 0.4. And thus, the SSAs can be classified as Cl-rich or Cl-depleted depending on their  $X_{(\text{Na,Mg})\text{Cl}}$   
273 values being greater or less than 0.4, respectively.

274

#### 275 3.3.1 Cl-rich SSAs

276 Fig. 4 displays the projected 2-dimensional (2-D) area ratio and optical images for Cl-rich SSAs  
277 #5 and #19 (panels a and d, respectively), and the 2-D area ratio of humidification (panels b and e) and  
278 dehydration (panels c and f) for the two SSAs as a function of RH. For SSAs #5 and #19 the mole



279 fraction of chloride,  $X_{(\text{Na},\text{Mg})\text{Cl}}$  was calculated to be 0.75 and 0.72, respectively. In addition, the figure  
280 also includes the (Na, Mg)(Cl, NO<sub>3</sub>) particle with  $X_{(\text{Na},\text{Mg})\text{Cl}} = 0.75$  for comparison.

281 During the humidification process, SSAs #5 and #19 initially remained constant in size until  
282 RH reached around 30%, after which they gradually increased in size. This behavior is also consistent  
283 with the (Na, Mg)(Cl, NO<sub>3</sub>) system (Figs. 4b and e), suggesting that MgCl<sub>2</sub>·6H<sub>2</sub>O (DRH = 33.3 %) or  
284 Mg<sup>2+</sup>-rich eutonic part may have undergone water absorption (Gupta et al., 2015a; Zieger et al., 2017).  
285 However, the deliquescence transitions were not as distinct as those in particles with  $X_{(\text{Na},\text{Mg})\text{Cl}} = 0.25$   
286 and 0.5 generated from (Na,Mg)(Cl,NO<sub>3</sub>) mixture solutions (see Fig. S3 in the Supporting Information).  
287 The size increase was followed by a shrinkage until RH = 60.5% due to structural rearrangement in the  
288 remaining undissolved salt-mixture crystals. Structural rearrangements are commonly observed after  
289 preliminary absorption of water at RHs just before the prompt deliquescence transition (Mikhailov et  
290 al., 2009; Mikhailov et al., 2004; Ahn et al., 2010; Gupta et al., 2015a; Gupta et al., 2015b). At first  
291 DRH = 63.8%, a partial droplet-like shape appeared in the particle morphology although there was no  
292 significant change in the 2-D area ratio. Clear final deliquescence transitions were observed in both  
293 SSAs #5 and #19 at DRHs = 73.5 % and 72.9 %, respectively, due to the dissolution of the remaining  
294 solid NaCl moiety in these Cl-rich particles. The measured DRHs of SSAs #5 and #19 were closer to  
295 the final DRHs calculated for the Na(Cl, NO<sub>3</sub>) system using the AIOMFAC model (Fig. 6), and higher  
296 than the calculated and measured ones in the (Na, Mg)(Cl, NO<sub>3</sub>) particles (Figs. 4b and e and Fig. 6).  
297 These observations for the Cl-rich SSAs suggest that most of the Mg<sup>2+</sup> salts (MgCl<sub>2</sub>·6H<sub>2</sub>O with DRH  
298 = 33.3 %; Mg(NO<sub>3</sub>)<sub>2</sub> with DRH = 52%) have already dissolved at low RHs or undergone complexation  
299 with organic moieties (Eom et al., 2016), and the remaining NaCl and NaNO<sub>3</sub> moieties drove the  
300 deliquescence transition. The hygroscopic growth of both SSAs #5 and #19 was much smaller than that  
301 of the (Na, Mg)(Cl, NO<sub>3</sub>) system (Figs. 4b and e) when RH was raised to 91.4%, indicating the presence  
302 of a partitioning hydrophobic layer composed of organic surfactants that covered the aqueous salt  
303 droplets and inhibited water uptake (Eom et al., 2016; Cochran et al., 2016; Bertram et al., 2018; Lee  
304 et al., 2020).

305 During the dehydration process as RH decreased from ~91% to ~5%, both the SSA droplets  
306 showed a continuous shrinkage in size before their efflorescence. However, the rate of shrinkage was  
307 much smaller than that of pure inorganic surrogates, such as the (Na, Mg)(Cl, NO<sub>3</sub>) system with  
308  $X_{(\text{Na},\text{Mg})\text{Cl}} = 0.75$  (Figs. 4c and f), indicating that the hydrophobic surfactant layers covering the aqueous  
309 salt droplets potentially impeded the water evaporation. SSAs #5 and #19 showed one clear



310 efflorescence transition at RH = 50.5% and 45.0%, respectively (Figs. 4a and d). Interestingly, SSA #5  
311 ( $X_{(\text{Na},\text{Mg})\text{Cl}} = 0.75$ ) underwent a sharp decrease in size from RH = 50.9 – 50.5%, which is considerably  
312 higher than the ERH range of ~45 – 47% for pure NaCl particles (Martin, 2000; Ahn et al., 2010; Eom  
313 et al., 2014), and the first ERHs of either Na(Cl, NO<sub>3</sub>) (Fig. 7) or (Na, Mg)(Cl, NO<sub>3</sub>) (Figs. 4c and 7)  
314 systems. On the other hand, SSA #19 ( $X_{(\text{Na},\text{Mg})\text{Cl}} = 0.72$ ) first showed a small decrease in size at RH =  
315 63.8 – 60.8%, which is not a typical efflorescence transition, followed by a sharp decrease in size at  
316 RH = 45.8 – 45.0%, which is on the lower side of the ERH range for pure NaCl and slightly higher  
317 than the first ERHs of Na(Cl, NO<sub>3</sub>) and (Na, Mg)(Cl, NO<sub>3</sub>) systems (Figs. 4f and 7). The higher ERH  
318 at RH = 50.5 % in SSA #5 indicates heterogeneous efflorescence of the NaCl moiety, while the ERH =  
319 45.0% in SSA #19 suggests the homogeneous nucleation of NaCl moiety. Both SSA droplets showed  
320 just one decisive efflorescence transition at their ERHs, indicating co-crystallization of most aqueous  
321 inorganic salt moieties along with NaCl, pointing towards the likelihood that the SSAs with more  
322 complicated chemical compositions than the inorganic surrogate aerosols contain chemicals which can  
323 act as seeds, such as (Na, Ca)SO<sub>4</sub> crystals, for the complete crystallization at the efflorescence transition.  
324 These observations are substantiated by the distribution of S and O at the center and edge of the NaCl  
325 moiety in the X-ray maps obtained from the effloresced SSA particles #5 and #19, respectively (Fig.  
326 S4) (Li et al., 2014b; Gupta et al., 2015b). The apparent (not so sharp) decrease in size of SSA #19 at  
327 RH = 63.8 – 60.8% could be attributed to: (i) the sudden shrinkage of viscous organic moieties covering  
328 the aqueous salt droplet; or (ii) inhibited or slow water loss, probably due to a kinetic barrier to  
329 crystallization from amorphous/gel forming moieties such as MgSO<sub>4</sub>/Mg(NO<sub>3</sub>)<sub>2</sub>/(CH<sub>3</sub>SO<sub>3</sub>)<sub>2</sub>(Mg, Ca)  
330 (Xiao et al., 2008; Zhao et al., 2006; Zhang et al., 2004; Liu and Laskin, 2009); or (iii) a phase transition,  
331 such as heterogeneous efflorescence, had occurred, but the presence of viscous moieties (organics or  
332 Mg<sup>2+</sup>- organic complex) affected the relative 2-D size decrease on the TEM grid substrate.

333

### 334 3.3.2 Equimolar and Cl-depleted SSAs

335 Fig. 5 shows the plots of the projected 2-D area ratio and optical images for an equimolar SSA  
336 #23 (Fig. 5a) and a Cl-depleted SSA #11 (Fig. 5d), and 2-D area ratio of humidification (panels b and  
337 e) and dehydration (panels c and f) for the two SSAs as a function of RH. The calculated mole fractions  
338 of chloride,  $X_{(\text{Na}, \text{Mg})\text{Cl}}$  for SSAs #23 and #11 are 0.52 and 0.23, respectively. The figure also includes  
339 the (Na, Mg)(Cl, NO<sub>3</sub>) particles with  $X_{(\text{Na}, \text{Mg})\text{Cl}} = 0.5$  and 0.25 for comparison.



340 During the humidification process, both SSAs #23 and #11 remained relatively constant until  
341  $RH = \sim 50\%$ , unlike the  $(Na, Mg)(Cl, NO_3)$  surrogates, probably due to the decreased concentration of  
342  $MgCl_2 \cdot 6H_2O$ . The particle size then began to shrink until  $RH = \sim 59\%$ . Both SSAs exhibited two distinct  
343 deliquescence transitions. Partial deliquescence transitions occurred at  $RH = \sim 63.8\%$ , which is the  
344 MDRH for the mixture of soluble moieties in the ambient SSAs and was reported for the first time.  
345 Both SSAs exhibited two clear deliquescence transitions. The observed and AIOMFAC-calculated  
346 MDRHs of the  $Na(Cl, NO_3)$  system are  $\sim 68\%$ , while the AIOMFAC-calculated second MDRH for the  
347  $(Na, Mg)(Cl, NO_3)$  system is  $66.5\%$  after the dissolution of  $MgCl_2 \cdot 6H_2O$  at the calculated first MDRH  
348 of  $\sim 34\%$ , as shown in Fig. 6. This indicates that the eutonic component in the ambient SSAs, with a  
349 lower MDRH of  $63.8\%$ , is composed of  $NaCl$ ,  $NaNO_3$ ,  $Mg(NO_3)_2$ , and some other minor, less-soluble  
350 moieties. The mutual deliquescence transition was more distinct in Cl-depleted SSAs than in Cl-rich  
351 SSAs, suggesting that the eutonic component in the ambient SSAs is richer with other salts compared  
352 to  $NaCl$ . As  $RH$  increased further, both SSAs #23 and #11 underwent final deliquescence transitions at  
353 DRHs =  $69.5\%$ . The observed DRH for SSA #23 ( $X_{(Na, Mg)Cl} = 0.52$ ) is closer to the final DRH calculated  
354 from AIOMFAC for pure  $NaCl$  moiety in the  $Na(Cl, NO_3)$  system (Fig. 6), and higher than the  
355 AIOMFAC-calculated final DRH for pure  $NaCl$  moiety in the  $(Na, Mg)(Cl, NO_3)$  system (Figs. 5b and  
356 6). The observed DRH for SSA #11 ( $X_{(Na, Mg)Cl} = 0.23$ ) is lower than the AIOMFAC-calculated final  
357 DRH (Fig. 6) for pure  $NaNO_3$  moiety in the  $Na(Cl, NO_3)$  system (Gupta et al., 2015b), and close to the  
358 AIOMFAC-calculated final DRH for pure  $NaNO_3$  moiety in the  $(Na, Mg)(Cl, NO_3)$  system (Figs. 5e  
359 and 6). The observation of Cl-depleted SSAs during humidification suggests that a  $(Na, Mg)(Cl, NO_3)$   
360 dominant system drives the deliquescence transition. As  $RH$  increased further, the hygroscopic growth  
361 of both SSAs #23 and #11 was stunted, in comparison to the inorganic multicomponent surrogates (Figs.  
362 5b and e), likely due to the presence of hydrophobic surfactants covering the aqueous salt droplet.

363 During the dehydration process, both SSAs #23 and #11 showed slower rates of shrinkage  
364 compared to the pure inorganic surrogates (Figs. 5c and f), suggesting inhibition of water evaporation  
365 due to surface hydrophobic organic moieties. The diffraction patterns at the aqueous salt droplet-  
366 organic surfactant interface were more prominent in the form of color and/or ring-like patterns for  
367 equimolar and Cl-depleted SSAs (Figs. 5a and d), indicating that the hydrophobic organic film may  
368 become thicker or the concentration of organic surfactants may increase with aging. During dehydration,  
369 SSA #23, which is equimolar or slightly Cl-rich, showed one sharp transition at  $RH = 44.1-43.6\%$  and  
370 a gradual decrease in size thereafter until  $RH = 30.7\%$ , which is not considered an efflorescence



371 transition (Fig. 5a). The distinct ERH of 43.6% observed for SSA #23 was higher than the first ERHs  
372 of both Na(Cl, NO<sub>3</sub>) and (Na, Mg)(Cl, NO<sub>3</sub>) systems (Fig. 5c and 7), indicating possible homogeneous  
373 efflorescence of NaCl along with other salts on crystalline seeds such as (Ca, Na)SO<sub>4</sub> (Pósfai et al.,  
374 1995; Semeniuk et al., 2007; Wise et al., 2007), as shown in the X-ray maps in Fig. S5a. The remaining  
375 metastable amorphous/gel type NO<sub>3</sub><sup>-</sup> moieties and MgSO<sub>4</sub>·xH<sub>2</sub>O may be responsible for the gradual  
376 decrease in size after the efflorescence transition (Li et al., 2016). Cl-depleted SSA #11 showed two  
377 clear efflorescence transitions at RH = 44.1–39.6% and 24.6–23.9%, as shown in Fig. 5d. The first  
378 ERH of 39.6% measured for SSA #11 was also higher than the ERHs for both Na(Cl, NO<sub>3</sub>) and (Na,  
379 Mg)(Cl, NO<sub>3</sub>) systems, while the second ERH of 23.9% was close to and lower than the ERH range for  
380 pure NaCl in (Na, Mg)(Cl, NO<sub>3</sub>) and Na(Cl, NO<sub>3</sub>) systems, respectively (Figs. 5f and 7). The  
381 observations for Cl-depleted SSA #11 suggest that the first ERH was most probably due to the  
382 heterogeneous crystallization of the dominant NaNO<sub>3</sub> and/or Mg(NO<sub>3</sub>)<sub>2</sub> on mixed cation sulfate  
383 crystalline seeds such as (Ca, Na)SO<sub>4</sub>, while NaCl continued to homogeneously nucleate until the  
384 second ERH, where it crystallized at the center/core of the particle (Woods et al., 2013), as shown in  
385 the X-ray maps in Fig. S5b.

386

### 387 **3.3.3 Phase diagrams of ambient SSAs in correlation with Na(Cl, NO<sub>3</sub>) and (Na, Mg)(Cl, NO<sub>3</sub>)** 388 **surrogates systems**

389 The phase diagrams of ambient SSAs in correlation with Na(Cl, NO<sub>3</sub>) and (Na, Mg)(Cl, NO<sub>3</sub>)  
390 surrogate systems can show the relationship between the observed deliquescence and efflorescence  
391 behavior of the ambient SSAs and those of the simpler surrogate systems. The ambient SSAs have more  
392 complex compositions, but the simpler surrogate systems can help to identify the dominant salts and  
393 their behavior in the ambient SSAs. For example, the observation of Cl-depleted SSAs during  
394 humidification suggests that a (Na, Mg)(Cl, NO<sub>3</sub>) dominant system drives the deliquescence transition.  
395 This information can be useful in understanding the hygroscopic properties and behavior of  
396 atmospheric aerosols.

397

#### 398 **3.3.3.1 Deliquescence phase diagram**

399 Fig. 6 shows the experimentally measured DRHs for the ambient SSA particles and those of the  
400 (Na, Mg)(Cl, NO<sub>3</sub>) and Na(Cl, NO<sub>3</sub>) systems, calculated from the AIOMFAC model, plotted as a  
401 function of the mole fraction of chloride,  $f(X_{(\text{Na, Mg})\text{Cl}}$  or  $X_{\text{NaCl}}$ ).



402 The first MDRH of the (Na, Mg)(Cl, NO<sub>3</sub>) system, which was calculated from AIOMFAC, is  
403 34.2%, while the MDRH measured in laboratory-generated (Na, Mg)(Cl, NO<sub>3</sub>) particles is ~33.4% (Fig.  
404 S3). These values are attributed to the dominant MgCl<sub>2</sub>·6H<sub>2</sub>O eutonic component (Gupta et al., 2015a).  
405 In some Cl-rich SSAs, a gradual increase in size and a change in morphology were observed at RH =  
406 ~33%, indicating that they were in the partial aqueous phase (Figs. 4a and d). It is also possible that the  
407 gradual water uptake observed in SSAs at low RHs is due to amorphous inorganic moieties such as  
408 MgSO<sub>4</sub>·xH<sub>2</sub>O (Zhao et al., 2006; Xiao et al., 2008) and Mg(NO<sub>3</sub>)<sub>2</sub>·xH<sub>2</sub>O (Zhang et al., 2004), and/or  
409 water-soluble secondary organics such as carboxylate salts formed due to reactions of the (Na, Mg)Cl  
410 species with dicarboxylic acids, which are ubiquitous in the marine boundary layer (Laskin et al., 2012;  
411 Ghorai et al., 2014; Li et al., 2021). Wise et al. (2009) reported that ambient SSAs started changing in  
412 morphology at 36(±15)% RH.

413 For the (Na, Mg)(Cl, NO<sub>3</sub>) system, the eutonic composition is  $X_{(\text{Na}, \text{Mg})\text{Cl}} = 0.46$ , with a second  
414 MDRH of 66.5%, calculated from AIOMFAC, and a measured value of ~66.6(±0.4)% in the laboratory-  
415 generated (Na, Mg)(Cl, NO<sub>3</sub>) particles (Fig. S3). For the Na(Cl, NO<sub>3</sub>) system, the eutonic composition  
416 is  $X_{\text{NaCl}} = 0.38$ , with the MDRH of 67.9%, calculated from AIOMFAC, and a measured value of  
417 ~67.9(±0.3)% in the laboratory-generated particles (Gupta et al., 2015b). The observed MDRH of  
418 63.8(±0.3)% for the ambient SSAs (Fig. 6) is slightly lower than those of the surrogate systems,  
419 indicating that the eutonic component in the mutual deliquescence transition may be Na(Cl, NO<sub>3</sub>)-rich,  
420 with minor concentrations of other soluble salt moieties, as the MDRH of salt mixtures is generally  
421 lower than individual salt DRHs (Wexler and Seinfeld, 1991). It is less likely that Na<sub>2</sub>SO<sub>4</sub> or CH<sub>3</sub>SO<sub>3</sub>Na  
422 are major components of the eutonic component in these ambient SSAs, as they have much higher  
423 MDRHs, i.e., MDRHs = 84.0% for Na(Cl, SO<sub>4</sub>) and 71% for Na(Cl, CH<sub>3</sub>SO<sub>3</sub>) (Chang and Lee, 2002;  
424 Liu and Laskin, 2009; Liu et al., 2011). The lowest final DRH measured for SSA #1 with  $X_{(\text{Na}, \text{Mg})\text{Cl}} =$   
425 0.33 is at RH = 65.4 % (Fig. 6), which is close to the observed MDRH of 63.8(±0.3)%, suggesting that  
426 the eutonic component likely has a chloride mole fraction within the range of  $X_{(\text{Na}, \text{Mg})\text{Cl}} = \sim 0.30\text{--}0.40$ .  
427 Interestingly, Wise et al. (2009) reported rounding in particle morphology at RH = 65(±4)%, which is  
428 close to the observed MDRH but was not confirmed as such since only four ambient SSA particles were  
429 studied.

430 The final DRHs in both (Na, Mg)(Cl, NO<sub>3</sub>) and Na(Cl, NO<sub>3</sub>) systems are solely determined by  
431 the solid salt remaining after the mutual deliquescence of the eutonic component. Fig. 6 clearly shows  
432 that for the Cl-rich SSA particles with  $X_{(\text{Na}, \text{Mg})\text{Cl}} > 0.40$ , which contain more NaCl than the eutonic





433 composition, the final DRH values (~67.5-73.5%) approached the DRH of pure NaCl salt (~75.3% at  
434 298 K) as the chloride concentration increased. Similarly, for the Cl-depleted particles with  $X_{(\text{Na},\text{Mg})\text{Cl}} <$   
435 0.40, the final DRH values (~65.4-72.9%) approached that of pure NaNO<sub>3</sub> salt (~74% at 298 K) as the  
436 chloride concentration decreased.

437 The chemical components of each phase in the ambient SSAs during the humidification process  
438 are not well known, therefore, five possible single and/or mixed phases are notated as alphabets (P, Q,  
439 R, S, and T) and the possible major chemical components in each phase (s = solid; aq = aqueous) are  
440 listed as follows:

- 441 (i) P-(s): all components are mixed in solid phase at  $\text{RH} < \sim 33\text{--}35\%$  at all mole fractions of chloride.  
442 (ii) Q-(s + aq): a mixed phase comprising possibly aqueous MgCl<sub>2</sub>·6H<sub>2</sub>O dominant eutonic  
443 components, and solid NaCl + (Na, Mg, Ca)(NO<sub>3</sub>, SO<sub>4</sub>) + organics between  $\text{RH} = \sim 33\%$  and  
444 the first clear MDRH of ~63.8%.  
445 (iii) R-(s + aq): a mixed phase comprising solid NaNO<sub>3</sub> + (Ca, Na)SO<sub>4</sub> and aqueous eutonic  
446 components rich in Na(Cl, NO<sub>3</sub>) + Mg(NO<sub>3</sub>, SO<sub>4</sub>, organics) between  $\text{RH} = 63.8\%$  and final  
447 DRHs for  $X_{(\text{Na},\text{Mg})\text{Cl}} < 0.40$ , i.e., Cl-depleted SSAs.  
448 (iv) S-(s + aq): a mixed phase comprising solid NaCl + (Ca, Na)SO<sub>4</sub> and aqueous eutonic  
449 components rich in Na(Cl, NO<sub>3</sub>) + Mg(Cl, NO<sub>3</sub>, SO<sub>4</sub>, organics) between the  $\text{RH} = 63.8\%$  and  
450 final DRHs for  $X_{(\text{Na},\text{Mg})\text{Cl}} > 0.40$ , i.e., Cl-rich SSAs.  
451 (v) T-(aq): aqueous phase for most components including NaCl + NaNO<sub>3</sub> + Mg(Cl, NO<sub>3</sub>, SO<sub>4</sub>,  
452 organics) above the measured final DRHs at all mole fractions of chloride, while (Ca, Na)SO<sub>4</sub>  
453 should remain in crystalline solid phase and does not take part in the deliquescence transitions  
454 in the measured RH range.

455

### 456 3.3.3.2 Efflorescence phase diagram

457 The experimentally measured ERHs for the ambient SSA particles and those of (Na, Mg)(Cl,  
458 NO<sub>3</sub>) and Na(Cl, NO<sub>3</sub>) systems are plotted as a function of the mole fraction of chloride,  $f(X_{(\text{Na},\text{Mg})\text{Cl}}$  or  
459  $X_{\text{NaCl}}$ ) in Fig. 7.

460 The first ERH values decrease from 44.5% to 24.8% and from 47.1% to 20.2% with decreasing  
461 mole fractions of chloride for  $X_{(\text{Na},\text{Mg})\text{Cl}} = 0.75$  to 0.25 in the (Na, Mg)(Cl, NO<sub>3</sub>) and  $X_{\text{NaCl}} = 0.9$  to 0.1  
462 in the Na(Cl, NO<sub>3</sub>) systems, respectively (Gupta et al., 2015b; Woods et al., 2013). This suggests that





463 the first efflorescence transitions in the surrogate systems are solely due to the homogeneous nucleation  
464 of NaCl for both Cl-rich and Cl-depleted particles, and that the amorphous (Na, Mg)NO<sub>3</sub> species cannot  
465 undergo homogeneous crystallization even at high supersaturation (Kim et al., 2012; Zhang et al., 2004).  
466 In the case of Cl-rich ( $X_{(\text{Na}, \text{Mg})\text{Cl}} > 0.40$ ) ambient SSAs, the first ERHs systematically decreased ranging  
467 from 50.5% to 33.0% due to the homogeneous nucleation of NaCl for most particles. However, for a  
468 few particles, such as SSA #5 (Fig. 4a, ERH = 50.5%), NaCl underwent heterogeneous crystallization  
469 on the mixed cation sulfate ((Ca, Na)SO<sub>4</sub>) crystalline seeds, resulting in higher ERH values. On the  
470 other hand, in Cl-depleted ( $X_{(\text{Na}, \text{Mg})\text{Cl}} < 0.40$ ) SSA particles, the first ERH values ranged from 46.0% to  
471 24.6% as a random set of values higher than the first ERHs in either surrogate system (Fig. 7), indicating  
472 heterogeneous crystallization of the richer (Na, Mg)NO<sub>3</sub> moieties on the mixed cation sulfate  
473 crystalline seeds for most particles.

474 The second/final ERH in the Na(Cl, NO<sub>3</sub>) system was only observed for Cl-rich particles ( $X_{\text{NaCl}} > 0.38$ )  
475 due to the mutual efflorescence of the eutonic component ( $X_{\text{NaCl}} = 0.38$ ) at MERH =  
476 ~30.0–35.5%, while no second ERH was recorded for Cl-depleted particles as NaNO<sub>3</sub> heterogeneously  
477 crystallized simultaneously on the homogeneously nucleated NaCl seeds (Gupta et al., 2015b). For the  
478 (Na, Mg)(Cl, NO<sub>3</sub>), a second ERH = ~29.6–27.4% was only observed for  $X_{(\text{Na}, \text{Mg})\text{Cl}} = 0.5$  among the  
479 three compositions measured (Fig. S3), probably due to the stochastic heterogeneous crystallization of  
480 the Na(Cl, NO<sub>3</sub>)-rich eutonic moiety on the NaCl seed. On the other hand, the typical transitions from  
481 30.5% to 17.9% for the second/final ERH in ambient SSAs were only observed for Cl-depleted particles  
482 with decreasing chloride concentration, i.e.  $X_{(\text{Na}, \text{Mg})\text{Cl}} = \sim 0.33$  to 0.15, indicating homogeneous  
483 nucleation of NaCl followed by assumed simultaneous heterogeneous crystallization of remaining  
484 aqueous salt moieties such as Mg(SO<sub>4</sub>, NO<sub>3</sub>).

485 In the laboratory-generated (Na, Mg)(Cl, NO<sub>3</sub>) particles with different mole fractions of  
486 chloride, i.e.  $X_{(\text{Na}, \text{Mg})\text{Cl}} = 0.25, 0.5, 0.75$  (Fig. S3), and 1.0 (Gupta et al., 2015a), clear final ERHs or  
487 MERHs were observed at low RHs ranging in 11.0–5.1% ( $X_{(\text{Na}, \text{Mg})\text{Cl}} = 0.25, 0.5$ , and 1.0) and 14.6–12.1%  
488 ( $X_{(\text{Na}, \text{Mg})\text{Cl}} = 0.75$ ), probably due to the crystallization of the dominant eutonic component of  
489 MgCl<sub>2</sub>·4H<sub>2</sub>O and MgCl<sub>2</sub>·6H<sub>2</sub>O, respectively. However, such low values of ERHs were not observed in  
490 the ambient SSAs, possibly because the concentrations of MgCl<sub>2</sub>·xH<sub>2</sub>O were too small to be detected  
491 by the optical microscopy-derived 2-D area ratio. On the other hand, the very gradual shrinkage



492 observed in ambient SSAs at low RHs may be due to the presence of amorphous  $\text{Mg}(\text{NO}_3, \text{SO}_4) \cdot x\text{H}_2\text{O}$   
493 moieties, which were present in some particles (e.g., SSAs #5, #19, and #23 in Figs. 4a, 4d, and 5a).

494 Considering the possibility of water content at low RHs during the dehydration process (Cziczo  
495 et al., 1997; Tang et al., 1997; Gupta et al., 2015a), the ambient SSAs can be divided into five potential  
496 phases, denoted as alphabets (P, Q, R, S, T), based on the presence of different chemical components  
497 and their states at different relative humidities (RHs) and the major chemical components in each phase  
498 (s = solid; aq = aqueous) are listed as follows:

499 (i) P-(aq): Almost all components, including NaCl,  $\text{NaNO}_3$ , and  $\text{Mg}(\text{Cl}, \text{NO}_3, \text{SO}_4, \text{organics})$ , are  
500 mixed in the aqueous phase at  $\text{RH} > \sim 55\%$  for all mole fractions of chloride. The  $(\text{Ca}, \text{Na})\text{SO}_4$   
501 should remain in the crystalline solid phase as it does not take part in the phase transitions within  
502 the measured RH range.

503 (ii) Q-(s + aq): a mixed phase including solid NaCl and other heterogeneously crystallized moieties  
504 + aqueous nucleating species like  $(\text{Mg} \cdot x\text{H}_2\text{O})^{2+}$  and  $\text{Cl}^-/\text{NO}_3^-/\text{SO}_4^{2-}$  at RHs  $< 50.5\%$  in Cl-rich  
505 SSAs ( $X_{(\text{Na}, \text{Mg})\text{Cl}} > 0.40$ ).

506 (iii) R-(s + aq): a mixed phase including heterogeneously crystallized  $(\text{Na}, \text{Mg})\text{NO}_3 \cdot x\text{H}_2\text{O}$  on  
507 crystalline  $(\text{Ca}, \text{Na})\text{SO}_4(x\text{H}_2\text{O})$  seeds + aqueous NaCl and other moieties, between the first  
508 ERHs = 46.0–24.6% and final ERHs = 30.5–17.9% for Cl-depleted SSAs ( $X_{(\text{Na}, \text{Mg})\text{Cl}} < 0.40$ ).

509 (iv) S-(s + aq): a mixed phase including solid  $(\text{Na}, \text{Mg}, \text{Ca})(\text{NO}_3, \text{SO}_4) \cdot x\text{H}_2\text{O}$  and homogeneously  
510 crystallized NaCl + aqueous/amorphous  $(\text{Mg} \cdot x\text{H}_2\text{O})^{2+}$  and  $\text{NO}_3^-/\text{SO}_4^{2-}$ , and other minor species  
511 below final ERHs = 30.5–17.9% for Cl-depleted SSAs ( $X_{(\text{Na}, \text{Mg})\text{Cl}} < 0.40$ ).

512 (v) T-(s): All components are mixed in solid phase at  $\text{RH} = \sim 14.6\text{--}5.0\%$  for all mole fractions of  
513 chloride. Amorphous or gel forming  $\text{Mg}(\text{NO}_3, \text{SO}_4) \cdot x\text{H}_2\text{O}$  shows gradual water loss, while only  
514 a small amount of  $\text{MgCl}_2 \cdot x\text{H}_2\text{O}$  is expected to crystallize.

515

### 516 3.4 Non-SSA particles

517 Generally, mineral particles such as aluminosilicates and calcium carbonate tend to be difficult  
518 to absorb water and grow in size with increasing RH. However, these particles can become hygroscopic  
519 after reaction with  $\text{NO}_x$  and  $\text{SO}_2$  in the presence of water and/or mixing with SSAs. Particle #14 shown  
520 in Fig. S6 is a highly aged aluminosilicate that has mixed with an SSA moiety, probably with  $(\text{Na},$   
521  $\text{Mg})(\text{Cl}, \text{NO}_3)$  and organic species as confirmed using X-ray spectrum. Clear deliquescence and



522 efflorescence transitions are observed in the gradual growth and shrinkage of particle #14 due mainly  
523 to the SSA part, and the growth of the aged aluminosilicate is certainly smaller than the SSA at  
524 maximum RH. Particle #20 shown in Fig. S7 is a reacted Ca-containing particle with nitrate showing  
525 gradual change in size during humidification and dehydration processes, following hygroscopic  
526 property reported before (Ahn et al., 2010). Particle #36 is a typical ammonium sulfate mixed with  
527 organic species as shown in Fig. S8, and the major chemical components of particle #36 are C, N, O,  
528 and S. The particle showed a first partial deliquescence transition at  $RH = 67.5\%$ , which may be the  
529 MDRH for the mixture of ammonium sulfate and organic species. Upon further increase in RH, the  
530 particle absorbed more moisture and fully dissolved at  $RH = 77.1\%$ , which is slightly lower than the  
531 DRH of pure ammonium sulfate particles (Wu et al., 2019). During the dehydration process, particle  
532 #36 showed a slower rate of shrinkage than ammonium sulfate particles, indicating inhibition of water  
533 evaporation due to surface hydrophobic organic moieties, and effloresced at  $RH = 27.6\%$ , which is  
534 lower than the ERH of ammonium sulfate particles (Wu et al., 2019). Some particles, such as reacted  
535 Ca-containing particles #17 and #25 and an aged  $SiO_2$  particle #37, exhibit partial dissolution as shown  
536 in Fig. S9 and S10. The 2-D area ratio of particle #17 at maximum RH is larger than that of particle  
537 #25, indicating the existence of more hygroscopic components in particle #17. Particle #37 showed  
538 gradual increase and decrease with partial dissolution only on the right side of particle, possibly due to  
539 the reacted Ca-containing one with nitrate moiety. The observation of the hygroscopic behavior of  
540 particles having partial growth suggests that a small content of hygroscopic chemical species can  
541 control the hygroscopic behavior of particles with major non-hygroscopic species. On the other hand,  
542 genuine aluminosilicate particles #29 and #32 (Fig. S11) and Fe-rich particles #2 and #7 (Fig. S12) did  
543 not show hygroscopic growth with changing RH.

544

#### 545 **4 Atmospheric Implications**

546 The investigation of the hygroscopic behavior of ambient SSAs is crucial for understanding the  
547 atmospheric chemistry and physics of marine environments. Previous studies have recognized that  
548 SSAs contain a wide range of inorganic sea salt and organic species (Schiffer et al., 2018), making it  
549 difficult to assess their hygroscopicity. In this study, the hygroscopic behavior of SSAs was  
550 systematically characterized and correlated with the role of inorganic salt moieties and enriched organic  
551 material coating. It was found that SSAs partially dissolve at lower RHs than the inorganic surrogates,  
552 including (Na, Mg)(Cl,  $NO_3$ ), due to the coexistence with other soluble moieties such as water-soluble



553 secondary organics. This indicates that SSAs will be increasingly susceptible to trace gas species and  
554 subsequent heterogeneous chemical reactions (Lee et al., 2020). The degree of chloride depletion was  
555 also found to affect the hygroscopic behavior of aged SSAs. SSAs with a higher degree of chloride  
556 depletion, i.e., higher aging degree, tend to exhibit multiple phase transitions with reducing RH,  
557 retaining phase-separated core-shell mixing state, which impacts aerosol-radiation interactions (Sun et  
558 al., 2018). The importance of considering these surrogate systems when modeling the hygroscopic  
559 behavior of ambient SSAs is apparent, especially in the case of field observations where a wide range  
560 of mixing states exist in particles. Even though there are still discrepancies regarding whether the  
561 organic fraction can influence the hygroscopic growth of SSAs, this study demonstrated that organic  
562 substances covering the sea salt moieties did suppress their hygroscopic growth. Further investigations,  
563 including obtaining exact elemental and molecular compositions of the organic shells, are needed to  
564 examine the aging of SSAs and quantify their uncertain effects on SSAs' hygroscopicity in  
565 thermodynamic models.

566 In addition, other species involving mineral dust and anthropogenic particles can be transported  
567 into marine environments and mixed with SSAs, which alter the particle compositions and in turn, their  
568 hygroscopicity. Heterogeneous mixing or coating of SSAs onto less hygroscopic dust particles can  
569 enhance their ability to interact with water vapor and reactive trace gases, leading to the formation of  
570 new particles and increased CCN activity (Tang et al., 2016). This mixing can also affect the optical  
571 properties and radiative forcing of atmospheric aerosols, as the scattering and absorption of solar  
572 radiation by aerosols are dependent on their size, composition, and mixing state. Furthermore, the  
573 impact of anthropogenic emissions on the hygroscopicity of marine aerosols is an important area of  
574 research, as increased levels of atmospheric pollutants may enhance the aerosol-water interaction and  
575 lead to changes in cloud properties and precipitation patterns (Su et al., 2022). Therefore, a  
576 comprehensive understanding of the hygroscopic behavior of marine aerosols and their interactions  
577 with other atmospheric constituents is necessary for accurately predicting their impacts on climate and  
578 air quality.

579

## 580 **5 Conclusions**

581 The hygroscopic behavior of individual ambient aerosol particles collected at a coastal site of  
582 Jeju Island, Korea, was investigated in correlation with their chemical compositions derived from X-  
583 ray microanalysis. Specifically, we focused on the hygroscopic behavior of ambient aged SSAs and



584 their dependence on the extent of reaction between  $\text{Cl}^-$  and  $\text{NO}_3^-$  ions, estimated from the mixing ratios  
585 of these ions using SEM-EDX. The phase transitions of the aged SSAs were found to be dominated by  
586 inorganics involving  $\text{Na}(\text{Cl}, \text{NO}_3)$  and/or  $(\text{Na}, \text{Mg})(\text{Cl}, \text{NO}_3)$  systems, with organic surfactant films  
587 covering the droplets suppressing hygroscopic growth and shrinkage with changing RH. For Cl-rich  
588 SSAs, two major transitions were observed during the humidification process, firstly at the MDRH and  
589 secondly at a final DRH. During the dehydration process, Cl-rich SSAs showed single-stage  
590 efflorescence. Cl-depleted SSAs showed two prompt deliquescence transitions during the  
591 humidification process and stepwise transitions during the dehydration process, depending on their  
592 chemical compositions.

593 The hygroscopic behavior of other particle types, including aged aluminosilicate, Ca-containing,  
594 organic and ammonium sulfate mixture, and Fe-rich particles, was also observed. Aged mineral  
595 particles showed varying degrees of size changes with changing RH, potentially due to the presence of  
596 SSAs and/or  $\text{NO}_3^-$  species resulting from coagulation and heterogeneous reactions, while non-reacted  
597 mineral and Fe-rich particles did not exhibit significant size changes during the hygroscopic process.  
598 The mixture particles of organic and ammonium sulfate displayed lower DRH and ERH values  
599 compared to pure ammonium sulfate salt, indicating the impact of organic species on the hygroscopic  
600 behavior of ammonium sulfate. While there have been some studies on the hygroscopic behavior of  
601 ambient marine aerosols, this study is one of the first to systematically investigate their hygroscopic  
602 behavior and to correlate it with their chemical compositions, providing better insights into their impact  
603 on climate change and atmospheric chemistry.

604

#### 605 **Data availability**

606 The data used in this study are available upon request; please contact Chul-Un Ro (curo@inha.ac.kr).

607

#### 608 **Author contributions**

609 LW, HJE, HY, DG, and HRC designed the experiment. LW, HJE, HY, and HRC carried out the  
610 measurements and/or analyzed the data. LW, HJE, HY, DG, HRC, PF, and CUR contributed  
611 discussion of the data. LW, HJE, DG, and CUR drafted the paper.

612

#### 613 **Competing interests**

614 The authors declare that they have no conflict of interest.



615 **Acknowledgements**

616 This study was supported by the National Research Foundation of Korea (NRF) grant funded by the  
617 Korean government (MSIT) (No. 2021R1A4A1032579 and No. 2021R1A2C2004240) and by the  
618 National Institute of Environmental Research (NIER) funded by the Ministry of Environment (MOE)  
619 of Korea (NIER-2021-03-03-007).

620

621 **References**

- 622 Ahn, K.-H., Kim, S.-M., Jung, H.-J., Lee, M.-J., Eom, H.-J., Maskey, S., and Ro, C.-U.: Combined Use  
623 of Optical and Electron Microscopic Techniques for the Measurement of Hygroscopic Property,  
624 Chemical Composition, and Morphology of Individual Aerosol Particles†, *Anal. Chem.*, 82, 7999-  
625 8009, 10.1021/ac101432y, 2010.
- 626 Ansari, A. S. and Pandis, S. N.: Prediction of multicomponent inorganic atmospheric aerosol behavior,  
627 *Atmos. Environ.*, 33, 745-757, [http://dx.doi.org/10.1016/S1352-2310\(98\)00221-0](http://dx.doi.org/10.1016/S1352-2310(98)00221-0), 1999.
- 628 Atkinson, D. B., Radney, J. G., Lum, J., Kolesar, K. R., Cziczo, D. J., Pekour, M. S., Zhang, Q., Setyan,  
629 A., Zelenyuk, A., and Cappa, C. D.: Aerosol optical hygroscopicity measurements during the 2010  
630 CARES campaign, *Atmospheric Chemistry and Physics*, 15, 4045-4061, 10.5194/acp-15-4045-  
631 2015, 2015.
- 632 Bertram, T. H., Cochran, R. E., Grassian, V. H., and Stone, E. A.: Sea spray aerosol chemical  
633 composition: elemental and molecular mimics for laboratory studies of heterogeneous and  
634 multiphase reactions, *Chem Soc Rev*, 47, 2374-2400, 10.1039/c7cs00008a, 2018.
- 635 Carslaw, K. S., Clegg, S. L., and Brimblecombe, P.: A Thermodynamic Model of the System HCl-  
636 HNO<sub>3</sub>-H<sub>2</sub>SO<sub>4</sub>-H<sub>2</sub>O, Including Solubilities of HBr, from <200 to 328 K, *J. Phys. Chem.*, 99,  
637 11557-11574, 10.1021/j100029a039, 1995.
- 638 Chan, C. K., Ha, Z., and Choi, M. Y.: Study of water activities of aerosols of mixtures of sodium and  
639 magnesium salts, *Atmos. Environ.*, 34, 4795-4803, [http://dx.doi.org/10.1016/S1352-  
640 2310\(00\)00252-1](http://dx.doi.org/10.1016/S1352-2310(00)00252-1), 2000.
- 641 Chan, C. K., Liang, Z., Zheng, J. A., Clegg, S. L., and Brimblecombe, P.: Thermodynamic properties  
642 of aqueous aerosols to high supersaturation .1. Measurements of water activity of the system Na+  
643 Cl--NO<sub>3</sub>--SO<sub>4</sub>2--H<sub>2</sub>O at similar to 298.15 K, *Aerosol Sci. Technol.*, 27, 324-344,  
644 10.1080/02786829708965477, 1997.
- 645 Chang, S.-Y. and Lee, C.-T.: Applying GC-TCD to investigate the hygroscopic characteristics of mixed  
646 aerosols, *Atmos. Environ.*, 36, 1521-1530, [http://dx.doi.org/10.1016/S1352-2310\(01\)00546-5](http://dx.doi.org/10.1016/S1352-2310(01)00546-5),  
647 2002.
- 648 Clegg, S. L., Brimblecombe, P., and Wexler, A. S.: Thermodynamic Model of the System  
649 H<sup>+</sup>-NH<sub>4</sub><sup>+</sup>-SO<sub>4</sub><sup>2-</sup>-NO<sub>3</sub><sup>-</sup>-H<sub>2</sub>O at Tropospheric Temperatures, *J. Phys. Chem. A*, 102, 2137-2154,  
650 10.1021/jp973042r, 1998a.
- 651 Clegg, S. L., Brimblecombe, P., and Wexler, A. S.: Thermodynamic Model of the System  
652 H<sup>+</sup>-NH<sub>4</sub><sup>+</sup>-Na<sup>+</sup>-SO<sub>4</sub><sup>2-</sup>-NO<sub>3</sub><sup>-</sup>-Cl<sup>-</sup>-H<sub>2</sub>O at 298.15 K, *J. Phys. Chem. A*, 102, 2155-2171,  
653 10.1021/jp973043j, 1998b.
- 654 Cochran, R. E., Laskina, O., Jayarathne, T., Laskin, A., Laskin, J., Lin, P., Sultana, C., Lee, C., Moore,  
655 K. A., Cappa, C. D., Bertram, T. H., Prather, K. A., Grassian, V. H., and Stone, E. A.: Analysis of  
656 Organic Anionic Surfactants in Fine and Coarse Fractions of Freshly Emitted Sea Spray Aerosol,  
657 *Environ. Sci. Technol.*, 50, 2477-2486, 10.1021/acs.est.5b04053, 2016.





- 658 Cochran, R. E., Laskina, O., Trueblood, J. V., Estillore, A. D., Morris, H. S., Jayarathne, T., Sultana, C.  
659 M., Lee, C., Lin, P., Laskin, J., Laskin, A., Dowling, J. A., Qin, Z., Cappa, C. D., Bertram, T. H.,  
660 Tivanski, A. V., Stone, E. A., Prather, K. A., and Grassian, V. H.: Molecular Diversity of Sea Spray  
661 Aerosol Particles: Impact of Ocean Biology on Particle Composition and Hygroscopicity, *Chem*,  
662 2, 655-667, 10.1016/j.chempr.2017.03.007, 2017.
- 663 Cohen, M. D., Flagan, R. C., and Seinfeld, J. H.: Studies of concentrated electrolyte solutions using the  
664 electrodynamic balance. 3. Solute nucleation, *J. Phys. Chem.*, 91, 4583-4590,  
665 10.1021/j100301a031, 1987.
- 666 Cziczo, D. J., Nowak, J. B., Hu, J. H., and Abbatt, J. P. D.: Infrared spectroscopy of model tropospheric  
667 aerosols as a function of relative humidity: Observation of deliquescence and crystallization, *J.*  
668 *Geophys. Res. — Atmos.*, 102, 18843-18850, 10.1029/97jd01361, 1997.
- 669 Eom, H.-J., Gupta, D., Li, X., Jung, H.-J., Kim, H., and Ro, C.-U.: Influence of Collecting Substrates  
670 on the Characterization of Hygroscopic Properties of Inorganic Aerosol Particles, *Anal. Chem.*,  
671 86, 2648-2656, 10.1021/ac4042075, 2014.
- 672 Eom, H. J., Gupta, D., Cho, H. R., Hwang, H., Hur, S., Gim, Y., and Ro, C. U.: Single-particle  
673 investigation of summertime and wintertime Antarctic sea spray aerosols using low-Z particle  
674 EPMA, Raman microspectrometry, and ATR-FTIR imaging techniques, *Atmos. Chem. Phys.*  
675 *Discuss.*, 2016, 1-30, 10.5194/acp-2016-584, 2016.
- 676 Finlayson-Pitts, B. J. and Pitts, J. N.: Chemistry of the upper and lower atmosphere : theory,  
677 experiments, and applications, Academic Press, San Diego, xxii, 969 p. pp.2000.
- 678 Freney, E. J., Adachi, K., and Buseck, P. R.: Internally mixed atmospheric aerosol particles:  
679 Hygroscopic growth and light scattering, *Journal of Geophysical Research*, 115,  
680 10.1029/2009jd013558, 2010a.
- 681 Freney, E. J., Adachi, K., and Buseck, P. R.: Internally mixed atmospheric aerosol particles:  
682 Hygroscopic growth and light scattering, *J. Geophys. Res. — Atmos.*, 115, D19210,  
683 10.1029/2009jd013558, 2010b.
- 684 Ge, Z., Wexler, A. S., and Johnston, M. V.: Multicomponent Aerosol Crystallization, *J. Colloid Interface*  
685 *Sci.*, 183, 68-77, <http://dx.doi.org/10.1006/jcis.1996.0519>, 1996.
- 686 Ge, Z., Wexler, A. S., and Johnston, M. V.: Deliquescence Behavior of Multicomponent Aerosols, *J.*  
687 *Phys. Chem. A*, 102, 173-180, 10.1021/jp972396f, 1998.
- 688 Geng, H., Hwang, H., Liu, X., Dong, S., and Ro, C. U.: Investigation of aged aerosols in size-resolved  
689 Asian dust storm particles transported from Beijing, China, to Incheon, Korea, using low-Z  
690 particle EPMA, *Atmos. Chem. Phys.*, 14, 3307-3323, 10.5194/acp-14-3307-2014, 2014.
- 691 Guo, L., Gu, W., Peng, C., Wang, W., Li, Y. J., Zong, T., Tang, Y., Wu, Z., Lin, Q., Ge, M., Zhang, G.,  
692 Hu, M., Bi, X., Wang, X., and Tang, M.: A comprehensive study of hygroscopic properties of  
693 calcium- and magnesium-containing salts: implication for hygroscopicity of mineral dust and sea  
694 salt aerosols, *Atmospheric Chemistry and Physics*, 19, 2115-2133, 10.5194/acp-19-2115-2019,  
695 2019.
- 696 Gupta, D., Eom, H. J., Cho, H. R., and Ro, C. U.: Hygroscopic behavior of NaCl-MgCl<sub>2</sub> mixture  
697 particles as nascent sea-spray aerosol surrogates and observation of efflorescence during  
698 humidification, *Atmos. Chem. Phys.*, 15, 11273-11290, 10.5194/acp-15-11273-2015, 2015a.
- 699 Gupta, D., Kim, H., Park, G., Li, X., Eom, H. J., and Ro, C. U.: Hygroscopic properties of NaCl and  
700 NaNO<sub>3</sub> mixture particles as reacted inorganic sea-salt aerosol surrogates, *Atmos. Chem. Phys.*,  
701 15, 3379-3393, 10.5194/acp-15-3379-2015, 2015b.
- 702 Haywood, J. and Boucher, O.: Estimates of the direct and indirect radiative forcing due to tropospheric  
703 aerosols: A review, *Rev. Geophys.*, 38, 513-543, 10.1029/1999rg000078, 2000.





- 704 Herich, H., Kammermann, L., Friedman, B., Gross, D. S., Weingartner, E., Lohmann, U., Spichtinger,  
705 P., Gysel, M., Baltensperger, U., and Cziczo, D. J.: Subarctic atmospheric aerosol composition: 2.  
706 Hygroscopic growth properties, *J. Geophys. Res. — Atmos.*, 114, D13204, 10.1029/2008jd011574,  
707 2009.
- 708 Kim, H., Lee, M.-J., Jung, H.-J., Eom, H.-J., Maskey, S., Ahn, K.-H., and Ro, C.-U.: Hygroscopic  
709 behavior of wet dispersed and dry deposited NaNO<sub>3</sub> particles, *Atmos. Environ.*, 60, 68-75,  
710 <http://dx.doi.org/10.1016/j.atmosenv.2012.06.011>, 2012.
- 711 Kong, X., Wolf, M. J., Roesch, M., Thomson, E. S., Bartels-Rausch, T., Alpert, P. A., Ammann, M.,  
712 Prisle, N. L., and Cziczo, D. J.: A continuous flow diffusion chamber study of sea salt particles  
713 acting as cloud nuclei: deliquescence and ice nucleation, *Tellus B: Chemical and Physical  
714 Meteorology*, 70, 1-11, 2018.
- 715 Krieger, U. K., Marcolli, C., and Reid, J. P.: Exploring the complexity of aerosol particle properties and  
716 processes using single particle techniques, *Chem. Soc. Rev.*, 41, 6631-6662, 10.1039/c2cs35082c,  
717 2012.
- 718 Krueger, B. J., Grassian, V. H., Iedema, M. J., Cowin, J. P., and Laskin, A.: Probing Heterogeneous  
719 Chemistry of Individual Atmospheric Particles Using Scanning Electron Microscopy and Energy-  
720 Dispersive X-ray Analysis, *Anal. Chem.*, 75, 5170-5179, 10.1021/ac034455t, 2003.
- 721 Lee, H. D., Morris, H. S., Laskina, O., Sultana, C. M., Lee, C., Jayarathne, T., Cox, J. L., Wang, X.,  
722 Hasenecz, E. S., DeMott, P. J., Bertram, T. H., Cappa, C. D., Stone, E. A., Prather, K. A., Grassian,  
723 V. H., and Tivanski, A. V.: Organic Enrichment, Physical Phase State, and Surface Tension  
724 Depression of Nascent Core–Shell Sea Spray Aerosols during Two Phytoplankton Blooms, *ACS  
725 Earth and Space Chemistry*, 4, 650-660, 10.1021/acsearthspacechem.0c00032, 2020.
- 726 Li, W., Shao, L., Shi, Z., Chen, J., Yang, L., Yuan, Q., Yan, C., Zhang, X., Wang, Y., Sun, J., Zhang, Y.,  
727 Shen, X., Wang, Z., and Wang, W.: Mixing state and hygroscopicity of dust and haze particles  
728 before leaving Asian continent, *J. Geophys. Res. — Atmos.*, 119, 2013JD021003,  
729 10.1002/2013jd021003, 2014a.
- 730 Li, X., Wu, L., Lee, J.-S., and Ro, C.-U.: Hygroscopic behavior and chemical reactivity of aerosols  
731 generated from mixture solutions of low molecular weight dicarboxylic acids and NaCl, *Physical  
732 Chemistry Chemical Physics*, 23, 11052-11064, 10.1039/d1cp00590a, 2021.
- 733 Li, X., Gupta, D., Eom, H.-J., Kim, H., and Ro, C.-U.: Deliquescence and efflorescence behavior of  
734 individual NaCl and KCl mixture aerosol particles, *Atmos. Environ.*, 82, 36-43,  
735 <http://dx.doi.org/10.1016/j.atmosenv.2013.10.011>, 2014b.
- 736 Li, Y. J., Liu, P. F., Bergoend, C., Bateman, A. P., and Martin, S. T.: Rebounding hygroscopic inorganic  
737 aerosol particles: Liquids, gels, and hydrates, *Aerosol Science and Technology*, 51, 388-396,  
738 10.1080/02786826.2016.1263384, 2016.
- 739 Liu, Y. and Laskin, A.: Hygroscopic Properties of CH<sub>3</sub>SO<sub>3</sub>Na, CH<sub>3</sub>SO<sub>3</sub>NH<sub>4</sub>, (CH<sub>3</sub>SO<sub>3</sub>)<sub>2</sub>Mg, and  
740 (CH<sub>3</sub>SO<sub>3</sub>)<sub>2</sub>Ca Particles Studied by micro-FTIR Spectroscopy, *J. Phys. Chem. A*, 113, 1531-1538,  
741 10.1021/jp8079149, 2009.
- 742 Martin, S. T.: Phase Transitions of Aqueous Atmospheric Particles, *Chem. Rev.*, 100, 3403-3454,  
743 10.1021/cr990034t, 2000.
- 744 Meskhidze, N., Petters, M. D., Tsigaridis, K., Bates, T., O'Dowd, C., Reid, J., Lewis, E. R., Gantt, B.,  
745 Anguelova, M. D., Bhave, P. V., Bird, J., Callaghan, A. H., Ceburnis, D., Chang, R., Clarke, A.,  
746 de Leeuw, G., Deane, G., DeMott, P. J., Elliot, S., Facchini, M. C., Fairall, C. W., Hawkins, L.,  
747 Hu, Y., Hudson, J. G., Johnson, M. S., Kaku, K. C., Keene, W. C., Kieber, D. J., Long, M. S.,  
748 Mårtensson, M., Modini, R. L., Osburn, C. L., Prather, K. A., Pszenny, A., Rinaldi, M., Russell, L.



- 749 M., Salter, M., Sayer, A. M., Smirnov, A., Suda, S. R., Toth, T. D., Worsnop, D. R., Wozniak, A.,  
750 and Zorn, S. R.: Production mechanisms, number concentration, size distribution, chemical  
751 composition, and optical properties of sea spray aerosols, *Atmos. Sci. Lett.*, 14, 207-213,  
752 10.1002/asl2.441, 2013.
- 753 Mikhailov, E., Vlasenko, S., Niessner, R., and Pöschl, U.: Interaction of aerosol particles composed of  
754 protein and salts with water vapor: hygroscopic growth and microstructural rearrangement, *Atmos.*  
755 *Chem. Phys.*, 4, 323-350, 10.5194/acp-4-323-2004, 2004.
- 756 Mikhailov, E., Vlasenko, S., Martin, S. T., Koop, T., and Pöschl, U.: Amorphous and crystalline aerosol  
757 particles interacting with water vapor: conceptual framework and experimental evidence for  
758 restructuring, phase transitions and kinetic limitations, *Atmos. Chem. Phys.*, 9, 9491-9522,  
759 10.5194/acp-9-9491-2009, 2009.
- 760 Ming, Y. and Russell, L. M.: Predicted hygroscopic growth of sea salt aerosol, *J. Geophys. Res. —*  
761 *Atmos.*, 106, 28259-28274, 10.1029/2001jd000454, 2001.
- 762 Nguyen, Q. T., Kjær, K. H., Kling, K. I., Boesen, T., and Bilde, M.: Impact of fatty acid coating on the  
763 CCN activity of sea salt particles, *Tellus B: Chemical and Physical Meteorology*, 69, 1304064,  
764 2017.
- 765 Niedermeier, D., Wex, H., Voigtländer, J., Stratmann, F., Brüggemann, E., Kiselev, A., Henk, H., and  
766 Heintzenberg, J.: LACIS-measurements and parameterization of sea-salt particle hygroscopic  
767 growth and activation, *Atmos. Chem. Phys.*, 8, 579-590, 10.5194/acp-8-579-2008, 2008.
- 768 Pandis, S. N., Wexler, A. S., and Seinfeld, J. H.: Dynamics of Tropospheric Aerosols, *J. Phys. Chem.*,  
769 99, 9646-9659, 10.1021/j100024a003, 1995.
- 770 Pöschl, U. and Shiraiwa, M.: Multiphase Chemistry at the Atmosphere–Biosphere Interface Influencing  
771 Climate and Public Health in the Anthropocene, *Chem. Rev.*, 115, 4440-4475, 10.1021/cr500487s,  
772 2015.
- 773 Pósfai, M., Anderson, J. R., Buseck, P. R., and Sievering, H.: Compositional variations of sea-salt-mode  
774 aerosol particles from the North Atlantic, *J. Geophys. Res. — Atmos.*, 100, 23063-23074,  
775 10.1029/95jd01636, 1995.
- 776 Quinn, P. K., Collins, D. B., Grassian, V. H., Prather, K. A., and Bates, T. S.: Chemistry and Related  
777 Properties of Freshly Emitted Sea Spray Aerosol, *Chem. Rev.*, 10.1021/cr500713g, 2015.
- 778 Rosati, B., Christiansen, S., Dinesen, A., Roldin, P., Massling, A., Nilsson, E. D., and Bilde, M.: The  
779 impact of atmospheric oxidation on hygroscopicity and cloud droplet activation of inorganic sea  
780 spray aerosol, *Sci Rep*, 11, 10008, 10.1038/s41598-021-89346-6, 2021.
- 781 Schiffer, J. M., Mael, L. E., Prather, K. A., Amaro, R. E., and Grassian, V. H.: Sea Spray Aerosol: Where  
782 Marine Biology Meets Atmospheric Chemistry, *ACS Cent Sci*, 4, 1617-1623,  
783 10.1021/acscentsci.8b00674, 2018.
- 784 Schill, S. R., Collins, D. B., Lee, C., Morris, H. S., Novak, G. A., Prather, K. A., Quinn, P. K., Sultana,  
785 C. M., Tivanski, A. V., Zimmermann, K., Cappa, C. D., and Bertram, T. H.: The Impact of Aerosol  
786 Particle Mixing State on the Hygroscopicity of Sea Spray Aerosol, *ACS Central Science*, 1, 132-  
787 141, 10.1021/acscentsci.5b00174, 2015.
- 788 Schindelholz, E., Risteen, B. E., and Kelly, R. G.: Effect of Relative Humidity on Corrosion of Steel  
789 under Sea Salt Aerosol Proxies: II. MgCl<sub>2</sub>, Artificial Seawater, *J. Electrochem. Soc.*, 161, C460-  
790 C470, 10.1149/2.0231410jes, 2014.
- 791 Seinfeld, J. H. and Pandis, S. N.: Atmospheric chemistry and physics : from air pollution to climate  
792 change, 2nd, J. Wiley & Sons Inc., Hoboken, N.J.2006.



- 793 Semeniuk, T. A., Wise, M. E., Martin, S. T., Russell, L. M., and Buseck, P. R.: Water uptake  
794 characteristics of individual atmospheric particles having coatings, *Atmos. Environ.*, 41, 6225-  
795 6235, <http://dx.doi.org/10.1016/j.atmosenv.2007.04.001>, 2007.
- 796 Song, Y., Li, J., Tsona, N. T., Liu, L., and Du, L.: Enrichment of short-chain organic acids transferred  
797 to submicron sea spray aerosols, *Sci Total Environ*, 851, 158122, 10.1016/j.scitotenv.2022.158122,  
798 2022.
- 799 Su, B., Wang, T., Zhang, G., Liang, Y., Lv, C., Hu, Y., Li, L., Zhou, Z., Wang, X., and Bi, X.: A review  
800 of atmospheric aging of sea spray aerosols: Potential factors affecting chloride depletion,  
801 *Atmospheric Environment*, 290, 10.1016/j.atmosenv.2022.119365, 2022.
- 802 Sun, J., Liu, L., Xu, L., Wang, Y., Wu, Z., Hu, M., Shi, Z., Li, Y., Zhang, X., Chen, J., and Li, W.: Key  
803 Role of Nitrate in Phase Transitions of Urban Particles: Implications of Important Reactive  
804 Surfaces for Secondary Aerosol Formation, *J. Geophys. Res.-Atmos.*, 123, 1234–1243,  
805 <https://doi.org/10.1002/2017jd027264>, 2018.
- 806 Tang, I. N., Tridico, A. C., and Fung, K. H.: Thermodynamic and optical properties of sea salt aerosols,  
807 *J. Geophys. Res. — Atmos.*, 102, 23269-23275, 10.1029/97jd01806, 1997.
- 808 Tang, M., Cziczko, D. J., and Grassian, V. H.: Interactions of Water with Mineral Dust Aerosol: Water  
809 Adsorption, Hygroscopicity, Cloud Condensation, and Ice Nucleation, *Chem Rev*, 116, 4205-4259,  
810 10.1021/acs.chemrev.5b00529, 2016.
- 811 ten Brink, H. M.: Reactive uptake of HNO<sub>3</sub> and H<sub>2</sub>SO<sub>4</sub> in sea-salt (NaCl) particles, *J. Aerosol Sci.*, 29,  
812 57-64, [http://dx.doi.org/10.1016/S0021-8502\(97\)00460-6](http://dx.doi.org/10.1016/S0021-8502(97)00460-6), 1998.
- 813 Tobon, Y. A., El Hajj, D., Seng, S., Bengrad, F., Moreau, M., Visez, N., Chiapello, I., Crumeyrolle, S.,  
814 and Choel, M.: Impact of the particle mixing state on the hygroscopicity of internally mixed  
815 sodium chloride-ammonium sulfate single droplets: a theoretical and experimental study, *Phys  
816 Chem Chem Phys*, 23, 14391-14403, 10.1039/d1cp01574e, 2021.
- 817 Vaishya, A., Ovadnevaite, J., Bialek, J., Jennings, S. G., Ceburnis, D., and O'Dowd, C. D.: Bistable  
818 effect of organic enrichment on sea spray radiative properties, *Geophysical Research Letters*, 40,  
819 6395-6398, 10.1002/2013gl058452, 2013.
- 820 Wang, J. and Martin, S. T.: Satellite characterization of urban aerosols: Importance of including  
821 hygroscopicity and mixing state in the retrieval algorithms, *J. Geophys. Res. — Atmos.*, 112,  
822 D17203, 10.1029/2006jd008078, 2007.
- 823 Wang, X., Deane, G. B., Moore, K. A., Ryder, O. S., Stokes, M. D., Beall, C. M., Collins, D. B.,  
824 Santander, M. V., Burrows, S. M., Sultana, C. M., and Prather, K. A.: The role of jet and film drops  
825 in controlling the mixing state of submicron sea spray aerosol particles, *Proc Natl Acad Sci U S  
826 A*, 114, 6978-6983, 10.1073/pnas.1702420114, 2017.
- 827 Wexler, A. S. and Clegg, S. L.: Atmospheric aerosol models for systems including the ions H<sup>+</sup>, NH<sub>4</sub><sup>+</sup>,  
828 Na<sup>+</sup>, SO<sub>4</sub><sup>2-</sup>, NO<sub>3</sub><sup>-</sup>, Cl<sup>-</sup>, Br<sup>-</sup>, and H<sub>2</sub>O, *J. Geophys. Res. — Atmos.*, 107, ACH 14-11-ACH 14-14,  
829 10.1029/2001jd000451, 2002.
- 830 Wexler, A. S. and Seinfeld, J. H.: Second-generation inorganic aerosol model, *Atmos. Environ.*, 27A,  
831 2731-2748, [http://dx.doi.org/10.1016/0960-1686\(91\)90203-J](http://dx.doi.org/10.1016/0960-1686(91)90203-J), 1991.
- 832 Wise, M. E., Semeniuk, T. A., Brientjes, R., Martin, S. T., Russell, L. M., and Buseck, P. R.:  
833 Hygroscopic behavior of NaCl-bearing natural aerosol particles using environmental transmission  
834 electron microscopy, *J. Geophys. Res. — Atmos.*, 112, D10224, 10.1029/2006jd007678, 2007.
- 835 Wise, M. E., Freney, E. J., Tyree, C. A., Allen, J. O., Martin, S. T., Russell, L. M., and Buseck, P. R.:  
836 Hygroscopic behavior and liquid-layer composition of aerosol particles generated from natural  
837 and artificial seawater, *J. Geophys. Res. — Atmos.*, 114, D03201, 10.1029/2008jd010449, 2009.



- 838 Woods, E., Chung, D., Lanney, H. M., and Ashwell, B. A.: Surface Morphology and Phase Transitions  
839 in Mixed NaCl/MgSO<sub>4</sub> Aerosol Particles, *J. Phys. Chem. A*, 114, 2837-2844, 10.1021/jp911133j,  
840 2010.
- 841 Woods, E., Heylman, K. D., Gibson, A. K., Ashwell, A. P., and Rossi, S. R.: Effects of NO<sub>y</sub> Aging on  
842 the Dehydration Dynamics of Model Sea Spray Aerosol, *J. Phys. Chem. A*, 117, 4214-4222,  
843 10.1021/jp401646d, 2013.
- 844 Wu, L., Li, X., and Ro, C.-U.: Hygroscopic Behavior of Ammonium Sulfate, Ammonium Nitrate, and  
845 their Mixture Particles, *Asian J. Atmos. Environ.*, 13, 196-211, 10.5572/ajae.2019.13.3.196, 2019.
- 846 Wu, L., Becote, C., Sobanska, S., Flaud, P.-M., Perraudin, E., Villenave, E., Song, Y.-C., and Ro, C.-  
847 U.: Hygroscopic behavior of aerosols generated from solutions of 3-methyl-1,2,3-  
848 butanetricarboxylic acid, its sodium salts, and its mixtures with NaCl, *Atmos. Chem. Phys.*, 20,  
849 14103-14122, 10.5194/acp-20-14103-2020, 2020.
- 850 Xiao, H.-S., Dong, J.-L., Wang, L.-Y., Zhao, L.-J., Wang, F., and Zhang, Y.-H.: Spatially Resolved  
851 Micro-Raman Observation on the Phase Separation of Effloresced Sea Salt Droplets, *Environ. Sci.*  
852 *Technol.*, 42, 8698-8702, 10.1021/es801181f, 2008.
- 853 Xu, W., Ovadnevaite, J., Fossum, K. N., Lin, C., Huang, R.-J., O'Dowd, C., and Ceburnis, D.: Aerosol  
854 hygroscopicity and its link to chemical composition in the coastal atmosphere of Mace Head:  
855 marine and continental air masses, *Atmospheric Chemistry and Physics*, 20, 3777-3791,  
856 10.5194/acp-20-3777-2020, 2020.
- 857 Zhang, X., Massoli, P., Quinn, P. K., Bates, T. S., and Cappa, C. D.: Hygroscopic growth of submicron  
858 and supermicron aerosols in the marine boundary layer, *Journal of Geophysical Research:*  
859 *Atmospheres*, 119, 8384-8399, 10.1002/2013jd021213, 2014.
- 860 Zhang, Y.-H., Choi, M. Y., and Chan, C. K.: Relating hygroscopic properties of magnesium nitrate to  
861 the formation of contact ion pairs, *J. Phys. Chem. A*, 108, 1712-1718, 2004.
- 862 Zhao, L.-J., Zhang, Y.-H., Wei, Z.-F., Cheng, H., and Li, X.-H.: Magnesium Sulfate Aerosols Studied  
863 by FTIR Spectroscopy: Hygroscopic Properties, Supersaturated Structures, and Implications for  
864 Seawater Aerosols, *J. Phys. Chem. A*, 110, 951-958, 10.1021/jp055291i, 2006.
- 865 Zieger, P., Vaisanen, O., Corbin, J. C., Partridge, D. G., Bastelberger, S., Mousavi-Fard, M., Rosati, B.,  
866 Gysel, M., Krieger, U. K., Leck, C., Nenes, A., Riipinen, I., Virtanen, A., and Salter, M. E.:  
867 Revising the hygroscopicity of inorganic sea salt particles, *Nat Commun*, 8, 15883,  
868 10.1038/ncomms15883, 2017.

869



870 **Figure 1.** Location of Gosan sampling site on Jeju Island, South Korea. (Map Copyright © Google Earth)



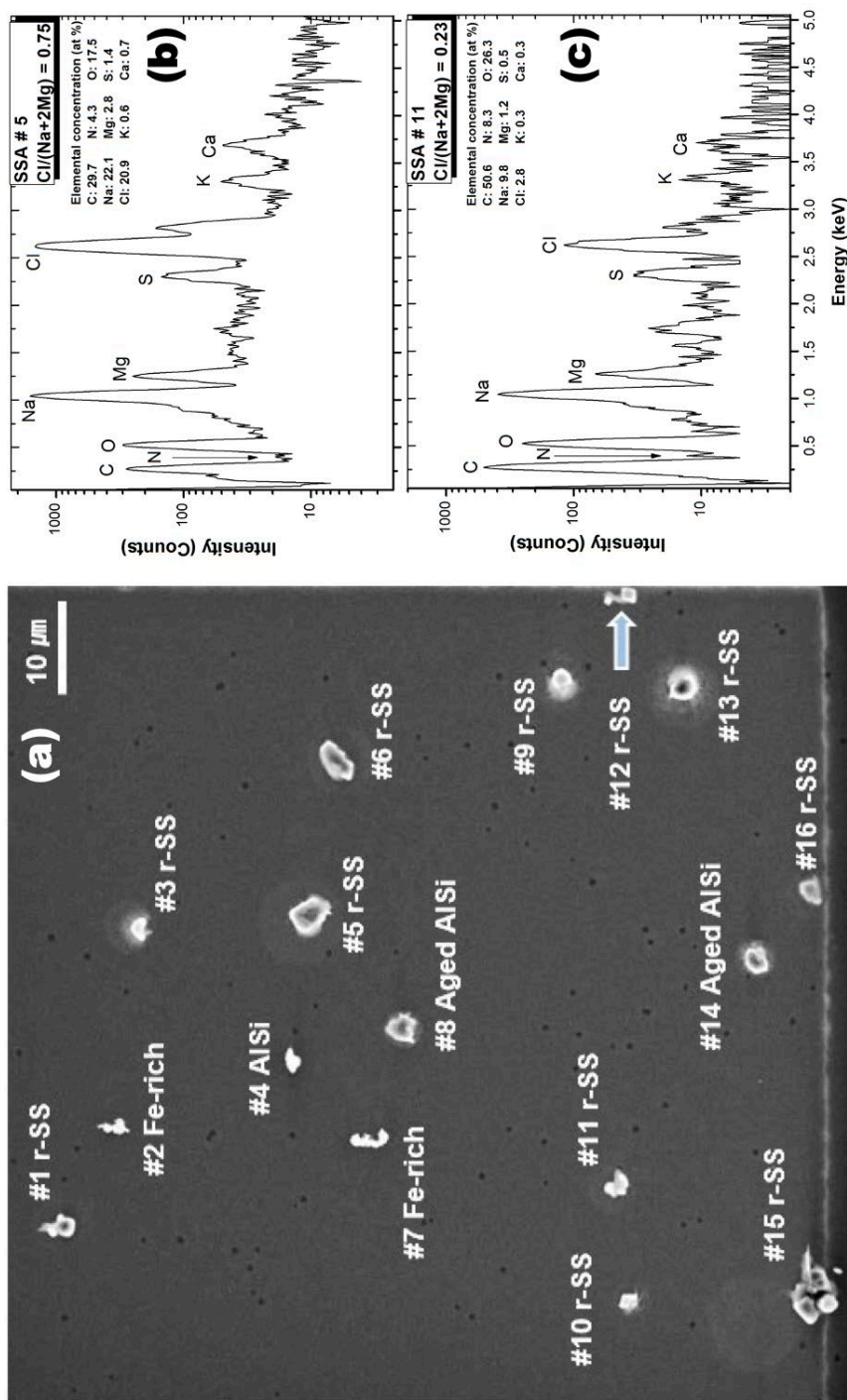
871

872



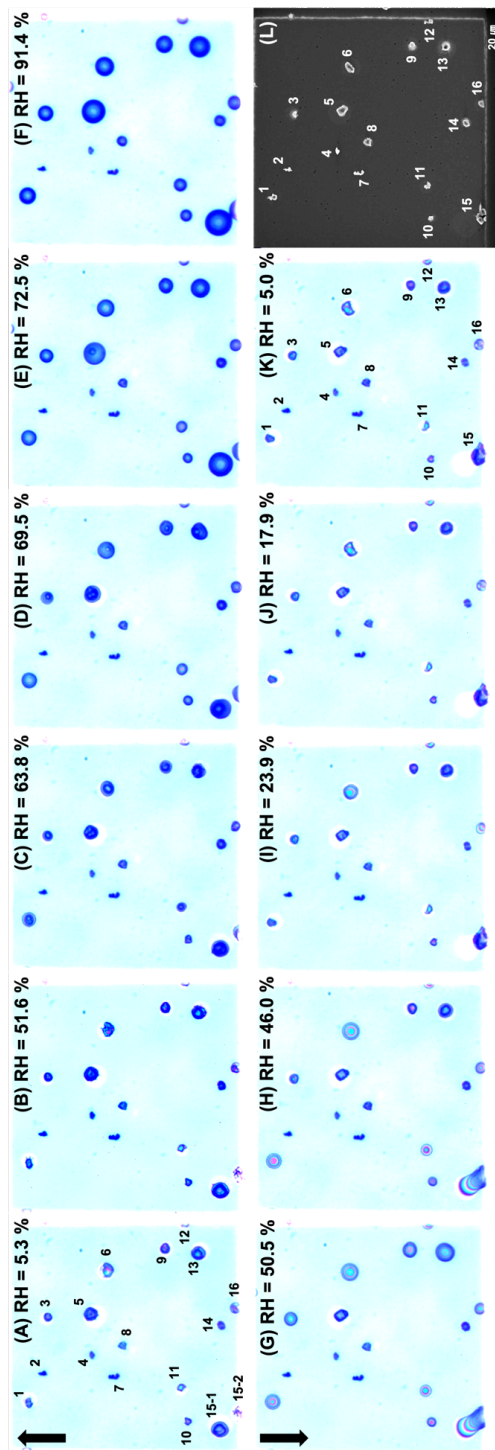


873 **Figure 2.** (a) Secondary electron image (SEI) of the first field containing 16 particles and X-ray spectra of (b) a Cl-rich and (c) a Cl-  
 874 depleted aged SSAs (particles #5 and #11, respectively). In this image, aged SSAs, Fe-containing particles, and aluminosilicates are  
 875 denoted as “r-SS”, “Fe-rich”, and “AlSi”, respectively.





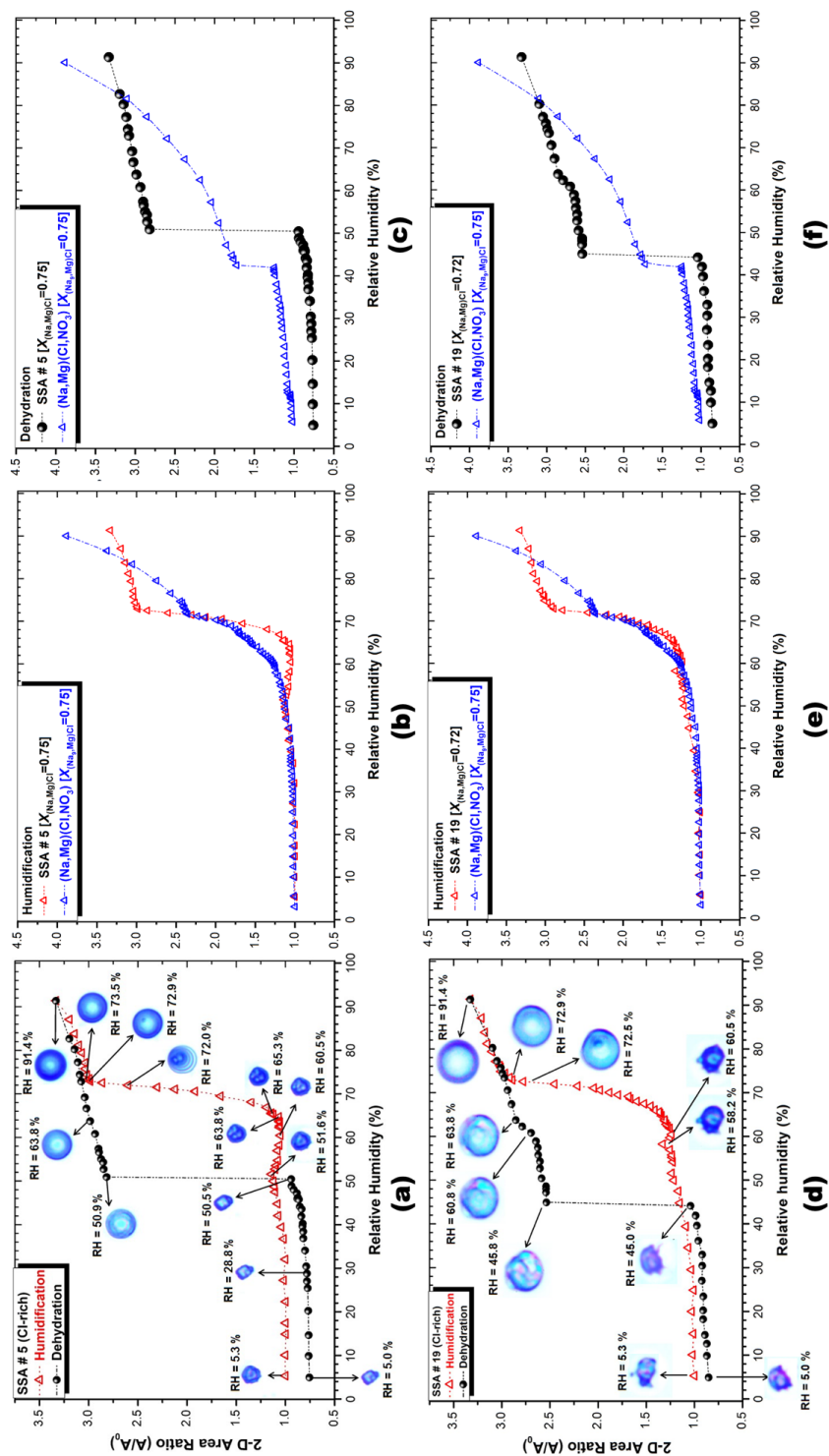
878 **Figure 3.** Optical images of the first field on TEM grid during humidifying (A-F, ↑) and dehydration (G-K, ↓) processes and the SEI  
879 of the same field (L).







881 **Figure 4.** 2-D area ratio plot and optical images of Cl-rich SSAs #5 and #19 (a and d), 2-D area ratio plots of humidification (b and e)  
 882 and dehydration (c and f) for the SSAs and (Na,Mg)(Cl,NO<sub>3</sub>) particle as a function of RH.



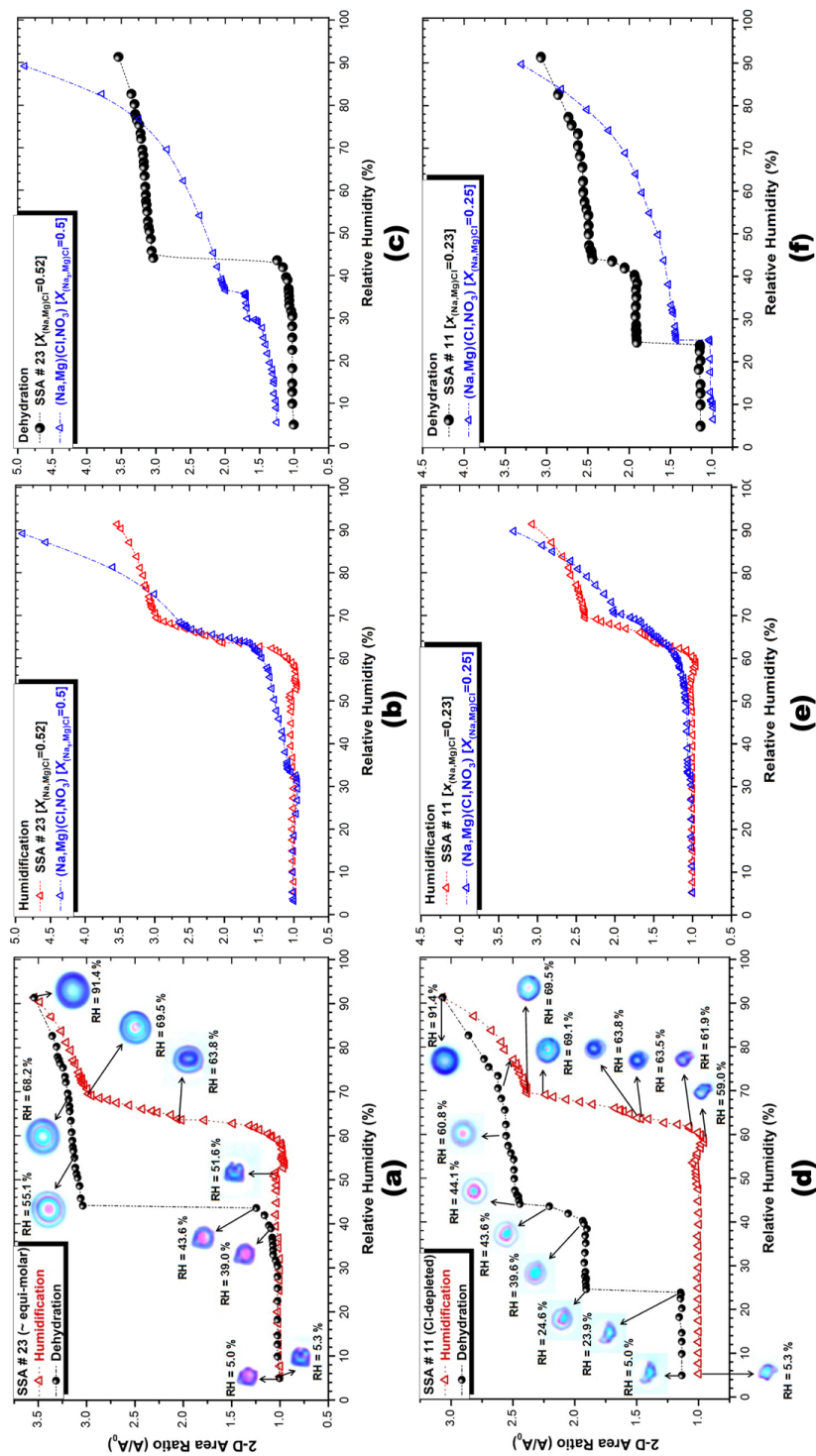
883

884

885



886 **Figure 5.** 2-D area ratio plot and optical images of an equimolar SSA #23 and a Cl-depleted SSA #11 (a and d), 2-D area ratio plots of  
 887 humidification (b and e) and dehydration (c and f) for the SSAs and (Na,Mg)(Cl,NO<sub>3</sub>) particles as a function of RH.



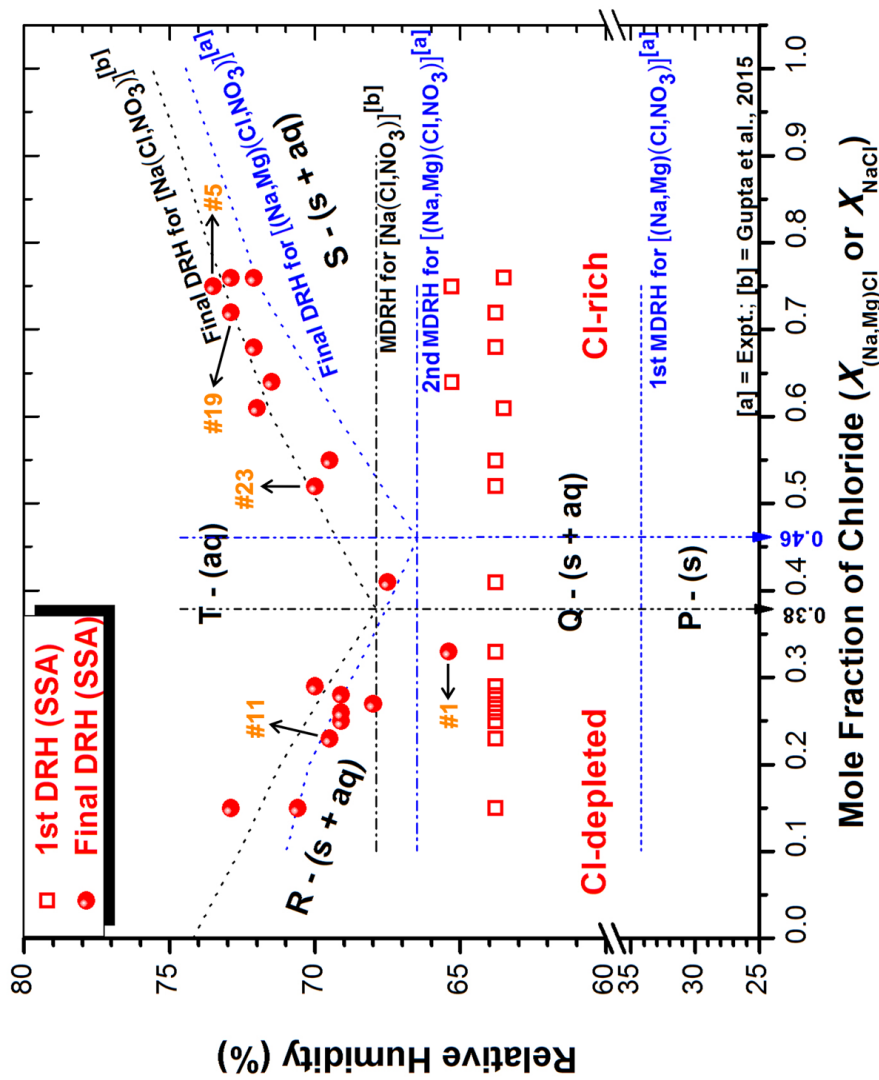
888

889

890



891 **Figure 6.** DRHs of ambient SSAs and (Na, Mg)(Cl, NO<sub>3</sub>) and Na(Cl, NO<sub>3</sub>) systems calculated from AIOMFAC plotted against the mole  
 892 fraction of chloride [ $X_{(Na, Mg)Cl}$  or  $X_{NaCl}$ ].





895 **Figure 7.** ERHs of ambient SSAs and those experimentally determined for (Na, Mg)(Cl, NO<sub>3</sub>) and Na(Cl, NO<sub>3</sub>) systems plotted against  
 896 the mole fraction of chloride [ $X_{(Na,Mg)Cl}$  or  $X_{NaCl}$ ].

